The Early Neoproterozoic Andean-Type Orogenic and Within-Plate Magmatic Events in the Northern Margin of the Yangtze Craton during the Convergence of the Rodinia Supercontinent

Yunxu Wei [1,2], Haiquan Li [3], Wenxiao Zhou [3,*], Changqian Ma [4], Ernest Chi Fru [5], Daliang Xu [1,2], Xin Deng [1,2], Mantang Tan [1,2], Xiaoming Zhao [6], Yang Xu [1,2] and Hao Liu [1,2]

[1] Wuhan Center, China Geological Survey (Geosciences Innovation Center of Central South China), Wuhan 430205, China; wyx1856@163.com (Y.W.); xdl2003geo@163.com (D.X.); cugxd@163.com (X.D.); tanmantang@sina.cn (M.T.); xuyang_0112@163.com (Y.X.); liuhao@163.com (H.L.)
[2] Research Center of Granitic Diagenesis and Mineralization, China Geological Survey, Wuhan 430205, China
[3] Institute of Geological Survey, China University of Geosciences, Wuhan 430074, China; lhq@cug.edu.cn
[4] Faculty of Earth Sciences, China University of Geosciences, Wuhan 430074, China; cqma@cug.edu.cn
[5] School of Earth and Environmental Sciences, Centre for Geobiology and Geochemistry, Cardiff University, Cardiff CF10 3AT, Wales, UK; chifrue@cardiff.ac.uk
[6] Institute of Karst Geology, China Geological Survey, Guilin 541004, China; zxm20040021@163.com
[*] Correspondence: zhouwenxiao@cug.edu.cn; Tel.: +86-27-67883017

Abstract: Although considered a crucial component of the Rodinia supercontinent, it remains uncertain how the Yangtze craton relates to the accretion and breakup of Rodinia. Here, the Huanglingmiao granitic complex (HGC), an intermediate-acid rock series that intruded on the southern Kongling terrane of the northern Yangtze craton margin, is investigated to help resolve this conundrum. Our analysis indicates that these rocks consist of tonalite, trondhjemite, granodiorite, oligoporphyritic granodiorite, porphyric biotite granodiorite, and fine- to medium-grained granodiorite dyke compositions. Collectively, this assemblage is further subdivided into two categories by their temporal, spatial, and geochemical features into early TTG-like and later granitic–dioritic units, which are composed of tonalite, trondhjemite, granodiorite, porphyritic granodiorite, and the fine- to medium-grained granodiorite dykes, respectively. Zircon U-Pb dating yields ages of 865~850 Ma for the TTG-like rocks, 844~825 Ma for the porphyritic granodiorites, and ~800 Ma for the granodiorite dykes. Combined with geochemical evidence, the data suggest that the early- and late-series rocks were formed by a partial melting of Mesoproterozoic and Paleoproterozoic crustal materials, respectively, suggesting that the vertical layering of the crust controlled the composition of the independent units. In addition, isotopic evidence points to different sources for the various rocks in the Kongling terrane and that mantle-derived materials influenced the early-series lithologies. Combined with previous studies on the northern margin of the Yangtze craton, it is inferred that the early-series rocks formed in an active continental margin environment, while the late-series rocks display within-plate boundary formation characteristics. The multiple magmatic activities revealed by this study record sequential partial melting with tectonic transition characteristics from an Andean-type to within-plate magmatism in the northern margin of the Yangtze craton. Taken together, these observations point to a strong association between these rocks, convergence, and incorporation of the northern Yangtze craton margin into the Rodinia supercontinent during the Tonian Period.

Keywords: Huanglingmiao granitic complex; geochemistry; Neoproterozoic; Yangtze craton; Rodinia supercontinent

1. Introduction

Accumulating evidence shows that the Yangtze craton (YC, Figure 1) and the Cathaysian block (CB) are tectonically related to the Rodinia supercontinent [1–12]. In the framework for the reconstruction of Rodinia [1–3,13–16], the northern margin of the YC is crucial for explaining oceanic and continental activities and later within-plate evolution [1,17]. For instance, oceanic subduction and within-plate extension activities are prevalent along the northern margin of the YC [18–27]. However, the geological records of Neoproterozoic orogeny, related oceanic subduction, within-plate extension processes, and the tectonic evolution of the YC remains incomplete. Furthermore, the location and tectonic features of the YC during Rodinia supercontinental convergence is ambiguous. Thus, systematic studies on tectonic evolution after oceanic subduction is required for the reconstruction of a complete tectonic history of the YC and its paleogeographical association with the Rodinia supercontinent.
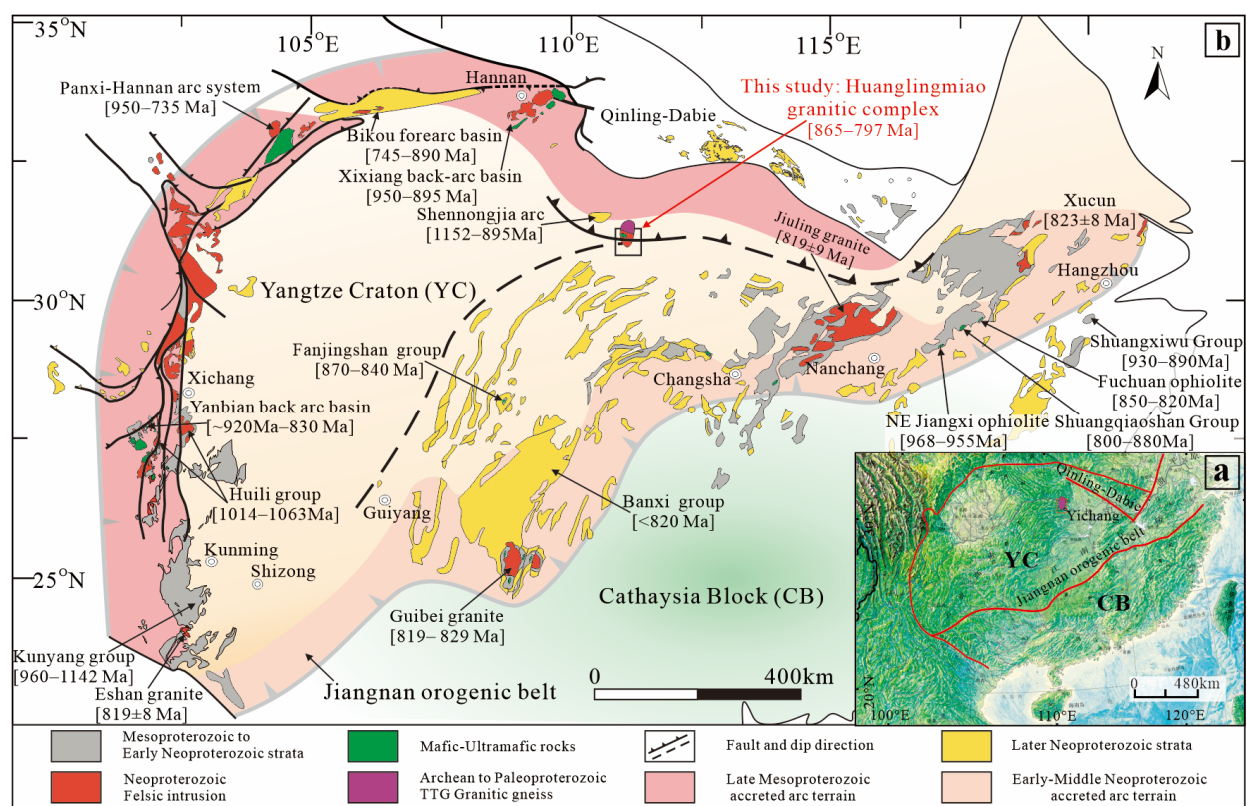

Figure 1. (**a**) A remote-sensing image of the South China craton and adjacent areas; (**b**) the distribution of Precambrian rocks in the Yangtze craton and Neoproterozoic tectonic framework. Modified after Zhao and Cawood [11] and Peng and Kusky [23].

Recent studies have indicated abundant Neoproterozoic magmatic activities in the northern margin of the YC (Figure 2) [18–27]. However, attempts to reconstruct the geological history of the YC in the Neoproterozoic have remained challenging because of the absence of orogeny-related metamorphic records. In this regard, studies on coeval granitic successions may prove to be crucial because of their wide temporal and spatial relationships [28,29]. Moreover, their formation could be associated with subduction, collision, and within-plate stage activities, as well as continental margin to continental nucleus areas [28,30–33]. In particular, the sequential partial melting of granitic rocks due to crustal thickening and the subsequent collapse and extensions [34] can provide abundant information that is vital for reconstructing the tectonic evolution of ancient orogenic belts. Recent works further show that the Kongling (KL) terrane is a crucial area in the northern margin of the YC due to the discovery of a series of well-preserved Archean to Neoproterozoic

magmatic [6,22,23,35–46]. In addition, the southern Kongling terrane (SKL, Figure 2) is associated with the major Neoproterozoic Huanglingmiao granitic complex (HGC) and its accessory mafic rocks. Thus, the SKL unquestionably represents a window through which the evolution of the YC during the Neoproterozoic can be studied.
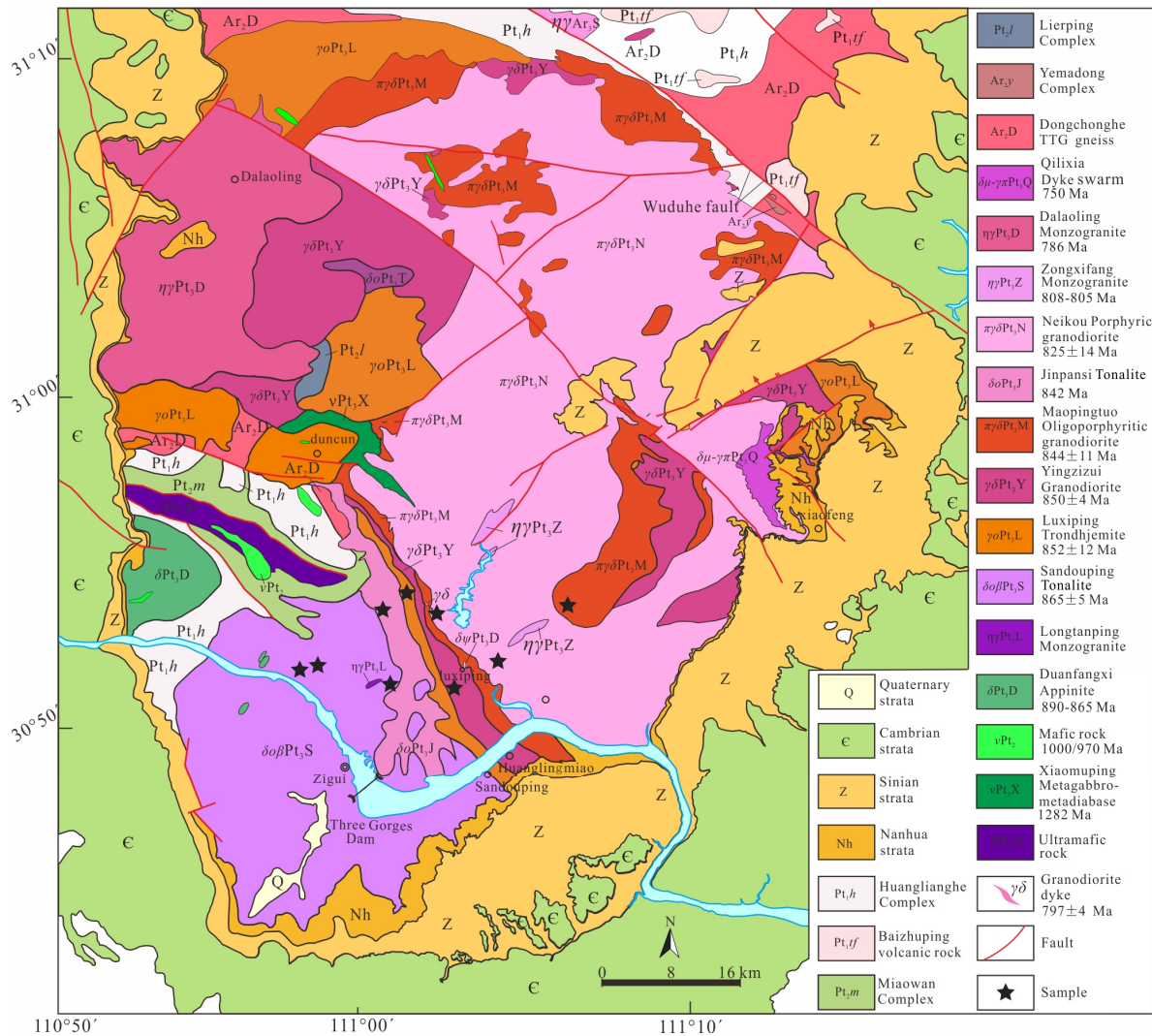

Figure 2. Geological map of the Huanglingmiao granitic complex and the distribution of related rocks in southern Kongling [27,47].

Most scholars believe that the HGC represents typical granitic lithologies that formed during the Neoproterozoic [6,16,25–27,48–52], and a variety of dating methods have been used to determine the formation age of the HGC, resulting in geochronological ages ranging from 863 to 800 Ma [27,52,53]. With regard to petrogenesis, there are three completely different views for the geodynamic environment of the KL terrane: some scholars believe that its formation occurred in a magmatic arc environment related to the southward subduction processes of the Qinling Ocean on the northern margin of the YC [27,48,54]. Some, however, hold the view that the formation age of the granites is related to a ~825 Ma Neoproterozoic mantle plume activity that occurred in South China that eventually led to the breakup of Rodinia [6,50,52,55,56]. Although there exist extensive studies on the HGC [16,25–27,48,49], the magmatic activities are more complex than is considered in the current consensus.

Here, we focus on the petrological, whole-rock, trace-elemental, geochronological, and Sr-Nd-Hf isotopic analyses of the HGC in the SKL of the northern margin of the YC to propose a complete tectonic history of the HGC. The results indicate that the HGC is divided into two series, and it is composed of early Sandouping tonalite, Luxiping trondhjemites, Yingzizui granodiorite, later Maopingtuo oligoporphyritic granodiorite, Neikou porphyric granodiorite, and granodiorite dyke. The two successions are associated with distinct provenance sources and evolutional trends. These petrogenetic observations may be indicative of a fingerprint of the larger-scale tectonic evolution of the YC.

2. Geological Setting and Petrological Characteristics

The KL terrane is the main body of the Huangling dome, which can be divided into northern Kongling (NKL) terrane and SKL terrane by the Wuduhe fault (Figure 2). The NKL terrane is characterized by Archean–Paleoproterozoic magmatic–tectonic records [39–46,57,58]. The SKL terrane is primarily characterized by Neoproterozoic magmatic–tectonic records [16,19–23,25–27,48,49,59]. As the main constituent of the SKL terrane, the HGC is distributed over an area of 570 km^2 (Figure 2). It intrudes on the Duanfangxi appinite suite and Miaowan ophiolitic mélange, as well as the Xiaoyicun, Dongchonghe, and Huanglianghe formations in the western area. Here, the HGC is overlain by the Nanhua System sediments in the south–southeastern belt—composed of the Liantuo and Nantuo formations. The Nanhua System rocks are intruded on by the Xiaofeng series to the eastern sector [48].

The fine-to-medium-grained HGC rocks are characterized by alternating dark gray to black and white laminations that exhibit a massive structure. A few enclaves (such as the Jingpansi tonalite) occur sporadically. Based on mineralogical composition, texture, and structure and contact relationships, the HGC has been subdivided into the Sandouping medium-grained biotite tonalite, the Luxiping fine-to-medium-grained trondhjemites (Luxiping trondhjemites), the Yingzizui medium-grained granodiorite (Yingzizui granodiorite), the Maopingtuo medium-grained oligoporphyritic granodiorite with few phenocrysts (Maopingtuo oligoporphyritic granodiorite), the Neikou medium-grained porphyric biotite granodiorite-porphyry (Neikou porphyric granodiorite), and the fine-to-medium-grained granodiorite dyke units [25].

2.1. Sandouping Tonalite

The Sandouping tonalite on the periphery of HGC displays a large batholith in the SW section of SKL, and it was intruded on by the Luxiping trondhjemites and Yingzizui granodiorite (Figure 2). The Sandouping tonalite sample is a fine-to-medium-grained biotite tonalite (Figure 3g). The grain size of the felsic minerals ranges from 0.1 to 2.5 mm, and the major minerals include plagioclase (40%), quartz (25%), biotite (10%), K-feldspar (5%), hornblende (10%), sericite (5%), and accessory minerals (2%), as detailed in Table S1. The 0.3–2.5 mm-tabular plagioclase crystals feature polysynthetic–pericline twinning, an andesine composition (An = 40–47%), and weak sericitization. Quartz crystals occur mostly as 0.1–1.5 mm allotriomorphic granular minerals, while columnar 1.2–/2.5 mm hornblende crystals display evident pleochroism. Biotite crystals are distributed in the intergranular pore space of other minerals.

2.2. Luxiping Trondhjemite

The Luxiping trondhjemite occurs as an annular ring in the Luxiping, Gehouping, and Lujiawan area on the margin of the HGC. The Luxiping trondhjemite crops out along an NNW-to-NW-trending zone and intrudes on the Jingpansi tonalite, Mesoproterozoic metamorphic strata, and basic–ultrabasic rocks (Figure 2). The Luxiping trondhjemite form mostly surge as intrusive contacts, and, less commonly, the intrusion contacts the Yingzizui granodiorite to the east and is overlain by an angular unconformity with the sedimentary rocks of Nanhua or Sinian formation. They always capture the Jingpansi tonalite and

Sandouping trondhjemite as enclaves. The texture of these enclaves are appinite-like, indicating their relatedness to the Duanfangxi appinite suite.
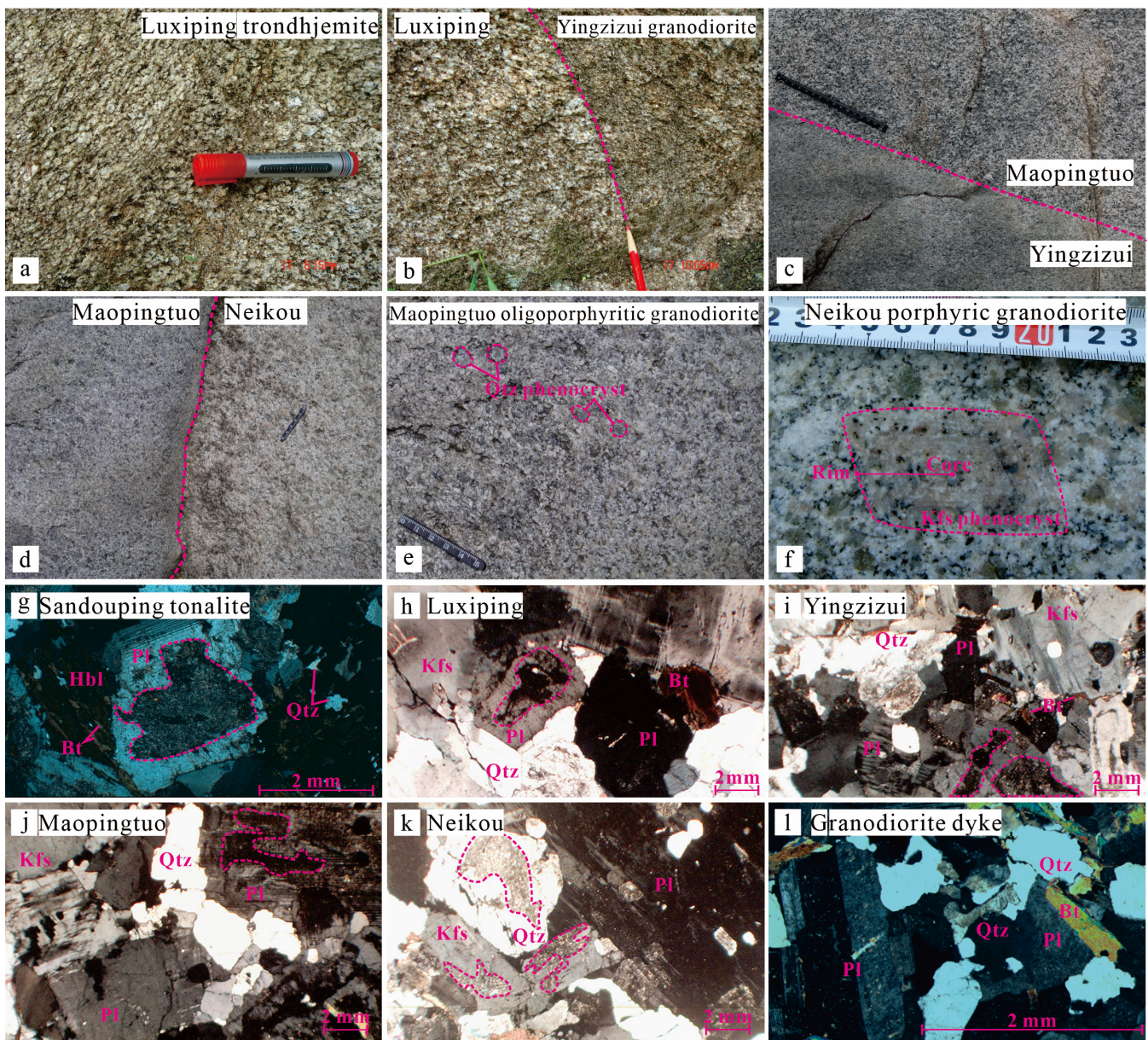

Figure 3. Field photographs and photomicrographs of the units that make up the Huanglingmiao granitic complex. (**a**) The Luxiping trondhjemite; (**b**) the Yingzizui granodiorite intruding into the Luxiping trondhjemite; (**c**) the Maopingtuo oligoporphyritic granodiorite intruding into the Yingzizui granodiorite; (**d**) the Neikou porphyric granodiorite intruding into the Maopingtuo oligoporphyritic granodiorite; (**e**) a few quartz phenocrysts in the Maopingtuo oligoporphyritic granodiorite; (**f**) the zonal K-feldspar phenocryst in the Neikou porphyric granodiorite; (**g**–**l**) photomicrographs for panel's a-f, respectively. Qtz = quartzite; Bt = biotite; Kfs = K-feldspar; and Pl = plagioclase.

The Luxiping trondhjemite sample (Figure 2) showed a fine-to-medium-grained trondhjemite texture (Figure 3a,h). The grain size of the felsic minerals ranged from 1 to 2.5 mm, and the major minerals included 55–70% plagioclase, 24–30% quartz, 3–8% biotite, K-2–5% feldspar, 1–3% hornblende, and 0.1–0.5% muscovite, as detailed in Table S1. Plagioclase crystals are tabular, display polysynthetic–pericline twinning, are andesine in composition (An = 24–30), and exhibit weak sericitization on their surfaces. Biotite phenocrysts

have characteristic tabular-flake structures, while magnetite is the major accessory mineral, although monazite, garnet, and zircon are also present.

2.3. Yingzizui Granodiorite

The Yingzizui granodiorites principally crops out at the Yingzizui–Bijia Mountain belt, which is on the margin of the HGC. It is distributed as an annular ring between the Luxiping trondhjemite and the Maopingtuo oligoporphyritic granodiorite. It intrudes into the former and was later intruded on by the latter (Figure 2).

The lithology of the Yingzizui granodiorite (Figure 2) is of a medium-grained granodiorite composition (Figure 3b,c,i). Its mineral composition ranges from 2 to 5 mm, with the majority being greater than 3 mm, which includes 50–58% plagioclase, 25–30% quartz, 8–15% K-feldspar, and 4–5% biotite. Plagioclase crystals are characterized by their euhedral-to-subhedral tabular shape, with polysynthetic–pericline twinning and an andesine–oligoclase composition (An = 24–28) that is characterized by clayization and sericitization, which have replacement and metasomatic textures between muscovite and plagioclase crystals. Quartz crystals are mostly allotriomorphic, granular, and distributed in other minerals; they exhibit a wavy extinction and recrystallization that is caused by tectonization. K-feldspar grains are mostly phenocrysts, which are distributed in other minerals and commonly show grid twinning. Biotite phenocrysts have characteristic tabular-flake structures, and brown-to-pale-yellow pleochroism. The accessory minerals include magnetite, apatite, ilmenite, allanite, and zircon, as detailed in Table S1.

2.4. Maopingtuo Oligoporphyritic Granodiorite

Trending in the NW, the Maopingtuo oligoporphyritic granodiorites crops out in the Luxiping area, and the SN trend at Maopingtuo, which is in the mantle of the HGC, intrudes into the Yingzizui granodiorite and is then later intruded on by the Neikou porphyric granodiorite (Figure 2). It contains the diorite porphyritic enclaves (appinite-type rock) and mafic magmatic enclaves.

The lithology of the Maopingtuo oligoporphyritic granodiorite (Figure 2) exhibits a granitic–porphyritic texture and a massive structure with few phenocrysts. It includes ~8% phenocrysts and 90% matrix minerals (Figure 3c–e,j). The phenocrysts vary from 5–15 mm, are composed of ~5% quartz, minor ~3% plagioclase, and rare K-feldspar, as detailed in Table S1. The matrix minerals range from 2 to 5 mm, with a majority of 3 mm. The minerals include 50–55% plagioclase, 25–30% quartz, K-feldspar (3–8%), 3–5% biotite, and magnetite. Plagioclase crystals are characterized by their euhedral-to-subhedral tabular shape, polysynthetic–pericline twinning, and andesine–oligoclase compositions (An = 24–28), which have undergone obvious clayization and sericitization. In some parts of the Maopingtuo oligoporphyritic granodiorite, the rock composition is like that of the trondhjemite. The mineral assemblage is the characteristic feature used to distinguish it from the Yingzizui granodiorite.

2.5. Neikou Porphyric Granodiorite

The Neikou porphyric granodiorite is mainly distributed in the Letianxi–Guchengping–Zhongguzhai belt in the core and main body of the HGC. It has intruded into the Maopingtuo oligoporphyritic granodiorite (Figure 2), and it contains the enclaves of biotite schist, dioritic porphyrite, and porphyric porbiotite-quartz diorite.

The lithology of the Neikou porphyric granodiorite is medium-grained porphyric biotite granodiorite–porphyry (Figure 2), which exhibits a porphyritic texture and massive structure (Figure 2). It includes ~20% phenocrysts and 80% matrix minerals (Figure 3d,l). The phenocrysts sizes from 1–7 cm, is composed of ~12% K-feldspar, ~5% plagioclase crystals, and ~5% quartz, as detailed in Table S1. A zonal structure occurs in K-feldspar crystals (Figure 3f). The matrix minerals range from 2 to 4 mm and include 40–45% plagioclase, 20–25% quartz, 5–7% K-feldspar, and 3–5% biotite. The accessory minerals include magnetite, allanite, and zircon. With increasing K-feldspar content, the rocks become

monzonitic granite–porphyry in some regions of the intrusion. It can be distinguished from the Maopingtuo oligoporphyritic granodiorite by its >10% K-feldspar phenocryst content.

2.6. Granodiorite Dyke

The dyke-like granodiorites are intruding into other rocks (e.g., the Neikou unit) in many places. The lithology of the granodiorite (Figure 2) exhibits fine-to-medium-grained granitic texture and a massive structure (Figure 3l). The mineral sizes range from 1 to 4 mm, with a majority being 2–3 mm in size. The minerals include plagioclase (50–55%), quartz (30%), K-feldspar (<10%), and biotite (4–8%), as detailed in Table S1. Plagioclase crystals are characterized by their euhedral–subhedral tabular shapes and polysynthetic–pericline twinning. Quartz is mostly allotriomorphic, granular, and distributed in other minerals; it also records wavy extinction and evidence of recrystallization. The K-feldspar grains are mostly distributed in other minerals. The biotite phenocrysts have characteristic tabular-flake structures and brown-to-pale-yellow pleochroism.

3. Analytical Methods

3.1. LA-ICP-MS Zircon U–Pb Dating

U-Pb radiometric dating and zircon trace-element composition analysis of the Sandouping unit were simultaneously conducted by LA-ICP-MS at the State Key Laboratory of Continental Tectonics and Dynamics, Northwest University, Xi'an, China. Laser sampling was performed using a Geolas Pro laser ablation system consisting of a 193 nm wavelength with a maximum energy of 200 mJ. An Agilent 7500a ICP-MS instrument (Agilent, Santa Clara, CA, USA) was used to acquire in-signal intensities. Helium and argon were used as carrier and make-up gases, respectively, and they were mixed via a T-connector before injection into the ICP. Signal smoothing was performed by incorporating a "wire" signal-smoothing device with the laser ablation system. The laser spot size and frequency were set to 30 μm and 5 Hz, respectively. Zircon 91500 and glass NIST610 were used as the external standards for U-Pb dating and trace element calibration, respectively. Each analysis incorporated approximately 20–30 s background acquisition, followed by 50 s data collection. An Excel-based software package, GLITTER Ver.4.0, was used to perform offline selection and integration of the background and analyzed signal data, and time-drift correction and quantitative calibration was performed for the trace-element analysis and U-Pb dating. Concordia diagrams and weighted mean calculations were made using Isoplot/Ex_ver3 [60].

3.2. SHRIMP Zircon U–Pb Dating

Zircons from the Luxiping, Yingzizui, Maopingtuo, Neikou units, and granodiorite were separated using conventional heavy-liquid and magnetic techniques at the Zhongnan Mineral Resource Supervision and Testing Center of Ministry of Land and Resources (MLR). The zircon grains were dated using the SHRIMP II ion microprobe at the Beijing SHRIMP Center, Chinese Academy of Geological Sciences. Analytical procedures are described in Williams [61] and Wan and Li [62]. Elemental abundances and $^{206}Pb/^{238}U$ ratios were calibrated using M257 and TEM standards, respectively [61,62]. The U, Th, and Pb concentrations were calculated using the methods given in Claoué-Long and Zhang [63]. The common Pb was corrected using measured ^{204}Pb abundances. Individual analyses are presented as 1σ error boxes on concordia plots, and uncertainties in mean ages are quoted at the 95% confidence level (2σ).

3.3. Whole-Rock Geochemical Analyses

Major element abundances were obtained by chemical analysis. The trace elements of Sr, Ba, Rb, Nb, Zr, and Ga were determined by XRF on pressed powdered pellets. Other trace elements including REE, Y, Th, Hf, Ta, Sc, and Co were analyzed on a VG Elemental Plasma Quad 3 inductively coupled plasma-mass spectrometer (ICP-MS) at the Zhongnan Mineral Resource Supervision and Testing Center of MLR. The accuracies of the XRF

analyses were estimated to be 2% for major element concentrations of >0.5 wt.% and 5% for trace elements. The ICP-MS analyses yielded accuracies better than 5%.

3.4. Zircon Hf Isotopic Analyses

Zircon Hf isotope analysis was carried out in situ using a Newwave UP213 laser-ablation microprobe attached to a Neptune multi-collector ICP-MS at the Institute of Mineral Resources, Chinese Academy of Geological Sciences, Beijing. Instrumental conditions and data acquisition were comprehensively described by Wu and Yang [64] and Hou, Li [65]. A stationary spot was used for the present analyses, with a beam diameter of 55 μm depending on the size of the ablated domains. Helium was used as a carrier gas to transport the ablated sample from the laser-ablation cell to the ICP-MS torch via a mixing chamber mixed with Argon. In order to correct the isobaric interferences of the ^{176}Lu and ^{176}Yb on ^{176}Hf, ^{176}Lu/^{175}Lu = 0.02658 and ^{176}Yb/^{173}Yb = 0.796218 ratios were determined [63]. For instrumental mass-bias correction, Yb isotope ratios were normalized to ^{172}Yb/^{173}Yb of 1.35274 [63] and Hf isotope ratios to ^{179}Hf/^{177}Hf of 0.7325 using an exponential law. The mass-bias behavior of Lu was assumed to follow that of Yb, and the mass-bias correction protocol details are described in Wu, Yang [64] and in Hou [65]. Zircon GJ1 was used as the reference standard, with a weighted mean ^{176}Hf/^{177}Hf ratio of 0.282014 ± 0.000017 (2σ, n = 13) during routine analyses. It was close to a weighted mean ^{176}Hf/^{177}Hf ratio of 0.282013 ± 19 (2σ), as determined via the in situ analysis by Elhlou, Belousova [66].

3.5. Sr-Nd Isotopic Composition Analyses

Sr-Nd isotopic ratios were analyzed on a Triton TI mass spectrometer (Thermo Fisher Scientific, Waltham, MA, USA) operated in static mode at China and South China Mineral Resources Supervision and Inspection Center. Full details of the Rb-Sr and Sm-Nd analysis procedures were reported in Li et al. [67] and Ma et al. [68]. The ZkbzNd (JMC), GBW04419, and BCR-2 standards measured during the analytical course yielded the ^{143}Nd/^{144}Nd values of 0.511557 ± 6(2σ, n = 6), 0.512719 ± 5 (2σ, n = 1), and 0.512619 ± 2 (2σ, n = 1). The GBW04411 and the NIST SRM987 standards measured during the analytical course yielded the ^{87}Sr/^{86}Sr values of 0.759979 ± 6 (2σ, n = 1) and 0.710309 ± 4 (2σ, n = 5), respectively.

4. Results

4.1. Zircon U-Pb Dating

The shapes of the zircon grains displayed that most of these crystals have long or short columnar structures, with a small fraction being granular. The length/width ratios of the zircon grains vary significantly, but they mainly range between 1:1 and 4:1 (Figure 4) with a yellowish-brown color. Cathodoluminescence (CL) images of the transparent zircon crystals showed them to be euhedral, with oscillatory zonal textures typical of a magmatic origin.

4.1.1. Sandouping Tonalite

Thirty spots were analyzed on 27 crystals of Sample D110. The zircon grain particle sizes ranged from 100×200 to 250×450 μm with 1.5–4.0 length–width ratios. Most of them displayed euhedrally long prismatic shapes with visible oscillatory zoning (Figure 4a). We counted the other 29 results except for one data point that represented the inherited old age (Point 5.1). The Th and U content of these crystals ranged between 21.89 and 335.55 ppm and 41.15 and 299.78 ppm, respectively. The Th/U ratios were 0.43–1.12 (Table S2). The concordant data were all >99%. The ^{206}Pb/^{238}U-^{207}Pb/^{235}U-associated ages ranged from 848 Ma to 878 Ma, with an upper intercept at 870 ± 6 Ma (Figure 4a). Values near the upper intercept age were used to calculate the weighted average age, which was 865 ± 5 Ma with an MSWD of 0.15, where n = 22 (Figure 4a), and it was interpreted as the formation age of the Sandouping tonalite.
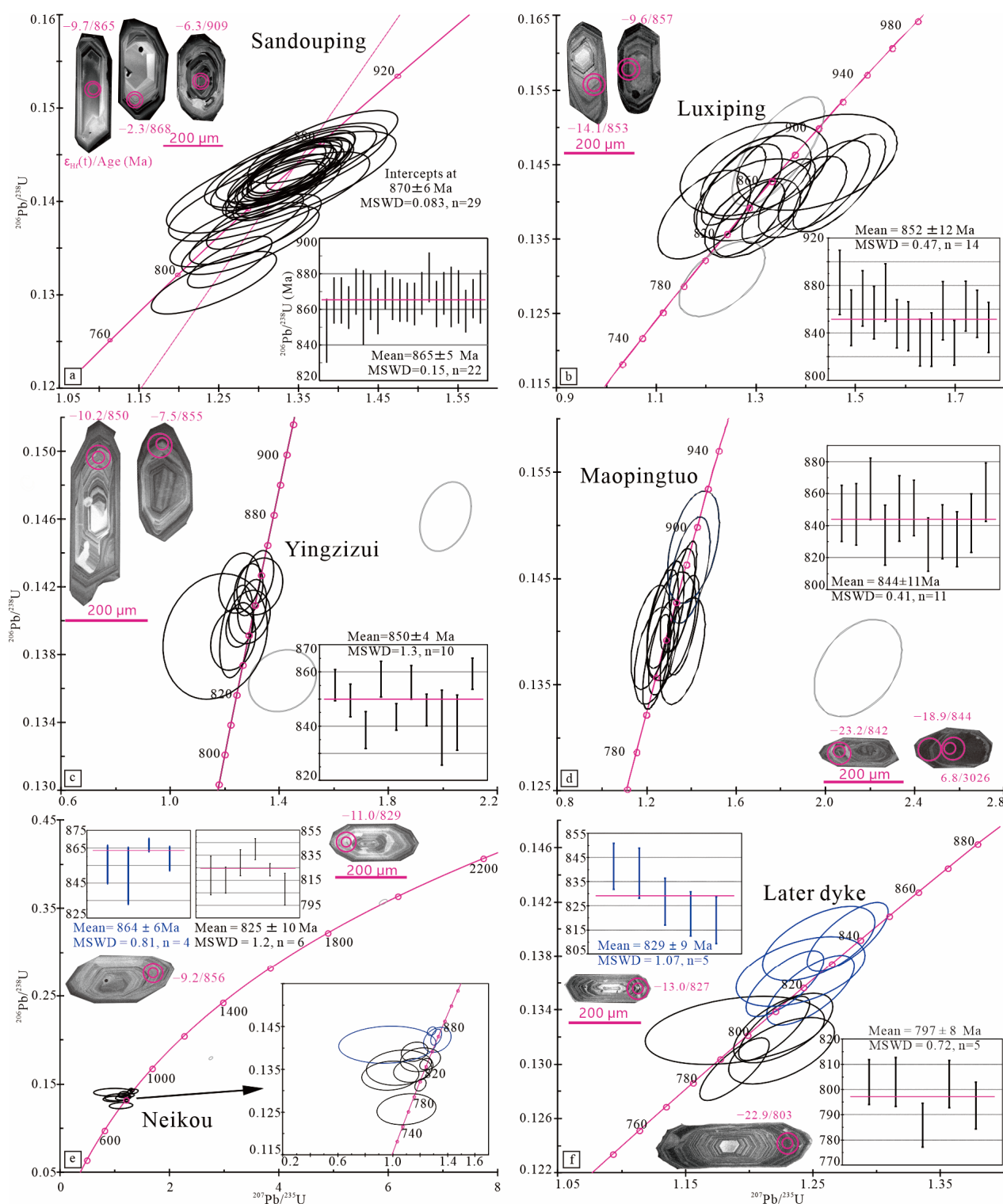
Figure 4. CL images of the representative zircon grains and zircon U-Pb-associated age diagrams (small spots represent the locations of U-Pb analyses, and large spots represent locations of the Lu-Hf analyses).

4.1.2. Luxiping Trondhjemite

A total of 15 spots were analyzed for the Luxiping trondhjemite PM054–12–1 sample. The U and Th concentrations of the zircon analytical points varied, ranging from 47 to 240 ppm and 13 to 145 ppm, respectively. The measured Th/U ratios mostly spanned

between 0.38 and 1.37 (with only three specimens yielding Th/U ratios between 0.11 and 0.16), which is consistent with those of typical magmatic zircons. The zircon ^{206}Pb/^{238}U ages varied between 786 Ma and 883 Ma (Table S3). The CL image (Figure 4b) depicts a clear black ring inside analytical Point #14, as well as white alteration margins and zones that partly cut through the zircon grain. This could have been caused by fluid intruding into the zircon through cracks in the late periods, resulting in Pb loss [69] and thus an artificially younger age of 786 ± 19 Ma. Therefore, this age was discarded when calculating the average ages. The zircon ^{206}Pb/^{238}U ages of the remaining 14 analytical points were relatively stable, varying between 832 Ma and 883Ma with a weighted average age of 852 ± 12 Ma (MSWD = 0.47, n = 14) (Figure 4b), which represents its formation age.

4.1.3. Yingzizui Granodiorite

For the Yingzizui granodiorite, the 12 data points analyzed for PM053–31–1 had U and Th concentrations ranging from 84 to 255 ppm and 49 to 234 ppm (except for one point that exhibited higher Th and U contents and a smaller Th/U ratio of 0.22 compared to the others), respectively. The Th/U ratios that mostly varied between 0.44 and 1.03 were consistent with those of typical magmatic zircons. The zircon ^{206}Pb/^{238}U ages spanned between 825 Ma and 879 Ma (Table S3). Imaging of the zircon grains containing analytical points of 5.1–5.2 by the CL images (Figure 4c) revealed a core–rim texture, while Point 5.1 displayed rhythmic zones characteristic of magmatic zircon, with a high ^{204}Pb content and a relatively younger age than most of the zircon grains. Point 5.2 located in the core had a distinct residual zircon protolith core that is surrounded by a corrosion texture, with Th and U concentrations that are relatively high and plot relatively far away from the concordant age. These two points were therefore excluded from further analyses. The remaining 10 points yielded relatively stable ^{206}Pb/^{238}U ages, varying between 839 and 857 Ma with a weighted average age of 850 ± 4 Ma (MSWD = 1.3, n = 10) (Figure 4c), which represents the formation age of the Yingzizui granodiorite.

4.1.4. Maopingtuo Oligoporphyritic Granodiorite

For the Maopingtuo oligoporphyritic granodiorite, 16 points were analyzed on Sample PM056–39–1. The U and Th concentrations for the points analyzed on these zircons ranged from 85 to 236 ppm and 53 to 211 ppm (with three yielding values between 303 and 535 ppm and 111 and 384 ppm), respectively. The Th/U ratios were mostly spread between 0.56 and 1.27 (with a single zircon core yielding a Th/U ratio of 0.27), which is consistent with those of typical magmatic zircons (Table S3). The CL images revealed a core–rim texture for the zircon grains with Points 6.1–6.2 and 13.1–13.2. Points 6.1 and 13.1 were found in the cores, with the residual cores belonging to protolith zircons. These were surrounded by corrosion textures with relatively high U concentrations and yielded ages of 1659 ± 32 Ma and 3026 ± 50 Ma, respectively. Point 14.2, located close to the rim of the zircon grains (Figure 4d), yielded a Pb content that was 5–10 times higher than that of the other analyzed spots; it also likely recorded a breakdown phenomenon, resulting in a relatively younger age of 825 ± 17 Ma. The cores of Zircons 5.1 and 9.1 exhibited corrosion textures, yielding significantly older ages of 889 ± 20 Ma and 877 ± 19 Ma, respectively. As these five analytical points probably reflect inherited zircons, they were excluded. The zircon ^{206}Pb/^{238}U ages for the remaining 11 analytical points were relatively stable, varying between 828 and 863 Ma with a weighted average age of 844 ± 11 Ma (MSWD = 0.41, n = 11) (Figure 4d), which represents the formation age of the Maopingtuo oligoporphyritic granodiorite.

4.1.5. Neikou Porphyric Granodiorite

For Sample PM056–12–1 from the Neikou porphyric granodiorite, a total of 14 points were analyzed. They had U and Th concentrations ranging from 32 to 435 ppm and 22 to 268 ppm (with values of 1345 to 314 and 251 to 428 ppm measured in the inherited core), respectively. Their Th/U ratios were mostly spread between 0.27 and 1.99, which

is consistent with those of typical magmatic zircons. The zircon ^{206}Pb/^{238}U ages varied between 763 Ma and 867 Ma (except for the two inherited cores, which yielded ages of 1968 ± 8 Ma and 1064 ± 5 Ma) (Table S3). According to the CL images (Figure 4e) zircon Points 11.1, 12.1, and 13.1 had relatively high U concentrations, with Points 11.1–11.2 and 13.1–13.2 displaying a core–rim texture. Points 11.1 and 13.1 in the zircon cores recorded corrosion textures, which are typical of early inherited zircons; their single-grain zircon ^{206}Pb/^{238}U ages were 1064 ± 5 Ma and 1968 ± 8 Ma, respectively. Point 11.2 was in the zircon rim and had unclear zoning, most likely because it was partially located close to the core; thus, the age (859 ± 7 Ma) was older than the normal zircons in that area. The younger zircon age (763 ± 14 Ma) of Point 3.1 possibly reflects thermal events or Pb loss that occurred at a later phase. The other 10 points yielded zircon ^{206}Pb/^{238}U ages that were relatively stable and were divided into two groups. A group of six points with a weighted average age of 825 ± 10 Ma (MSWD = 1.2) (Figure 4e) represented the formation age of the Neikou porphyric granodiorite. The weighted average age of the four other points of 864 ± 6 Ma (MSWD = 0.81), close to that of Point 11.2, fell between the Sandouping and Luxiping formation ages.

4.1.6. Granodiorite Dyke

For the granodiorite dyke Sample D3336–1, a total of 11 points were analyzed. The U and Th concentrations of the zircon grains ranged from 225 to 782 ppm and 102 to 588 ppm, respectively. The Th/U ratios mostly varied between 0.39 and 0.89 (except for the Th/U ratio of one inherited zircon grain, which was 0.25), all of them consistent with those of typical magmatic zircons. The zircon ^{206}Pb/^{238}U ages spanned between 794 Ma and 841 Ma (Table S3). The CL images (Figure 4f) suggest that the analyzed Point 11.1 had a core–rim texture. The core recorded a clear corrosion texture and the rim rhythmic zoning, thus exhibiting the features of magmatic zircons; the growth shape of the rim and inner zircon was not continuous with 'the old core-young rim' texture, indicating that the late-phase magma enclosure and growth occurred around the early core. The analytical point, located on the core–rim boundary of the zircon grains, yielded a measured age of 1734 ± 18 Ma, which represents mixed ages. The remaining 10 points from the rim—and the ages concentrated in the two groups, where one is represented by five zircon grains with an age of 829 ± 9 Ma (MSWD = 1.07)—were close to the formation age of the Neikou granodiorite. Five zircon grains in the other age group yielded a weighted-average age of 797 ± 8 Ma (MSWD = 0.72) (Figure 4f), which represents the formation age of the granodiorite dyke.

4.2. Geochemistry

The results of the chemical analyses of the HGC are shown in Table S4. There is a significant positive correlation between the SiO$_2$, alkaline, and differentiation index (DI, DI = Q + Or + Ab + Ne + Lc + Kp) of rock contents from early-to-late series, and it is negatively correlated with the contents of Fe, MgO, CaO, P$_2$O$_5$, and the Mg$^{\#}$ ratio (Figures 5 and 6). Further, the whole-rock major and trace-element composition, combined with field and geochronological results, were used to divide the lithologies into two groups. The early-series samples were characterized by low K$_2$O concentrations, and they were composed of the Sandongping unit, Luxiping unit, and Yingzizui unit; the late series were composed of the Maopingtuo unit and Neikou unit; and the late-series granodiorite dyke had high SiO$_2$ and K$_2$O contents. The early series showed the highest value of trace-elemental composition than the late-series intermediate concentrations. Notably, the trace-element content of the granodiorite dyke was close to the Luxiping unit and Yingzizui compositions, yet far from the concentrations recorded in the Maopingtuo and Neikou units.
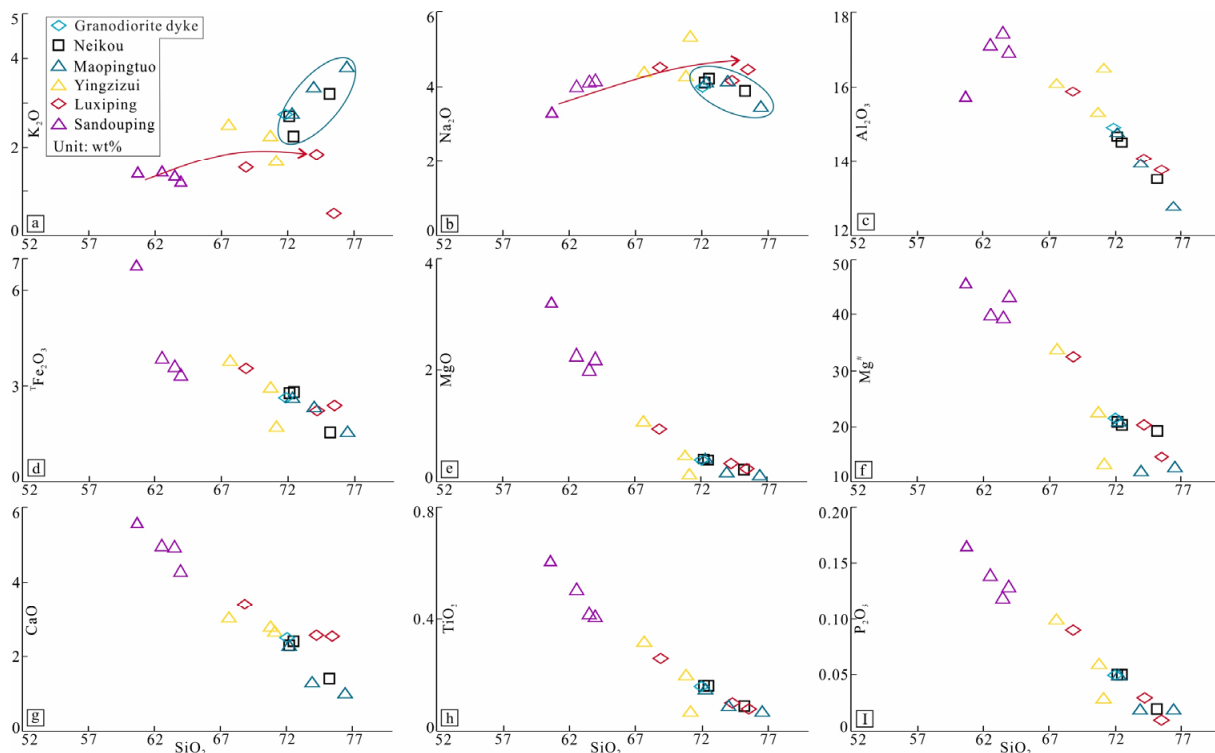
Figure 5. Harker diagrams of the selected major elements (**a–e**,**g–i**) and Mg$^{\#}$ (**f**) vs. SiO$_2$ contents for the Neoproterozoic Huanglingmiao granitic complex. The red lines display the relations of the early series for the Huanglingmiao granitic complex.

4.2.1. Major Elements

The early-series rocks were characterized by TTG-like contents. The Sandouping unit was characterized by low SiO$_2$ (60.69 wt.%), high iron (^{T}Fe$_2$O$_3$ = 6.76 wt.%), MgO (3.22 wt.%), CaO (5.61 wt.%), P$_2$O$_5$ (0.16 wt.%), TiO$_2$ content, and Mg$^{\#}$ ratio (45.89) (Figure 5). The corresponding K$_2$O + Na$_2$O was 4.80 wt.%, with Na$_2$O/K$_2$O and A/CNK ratios of 2.28 and 0.91. Its Q-A-P and alkaline-SiO$_2$ diagram (Figure 6a,b) suggests that it falls into the diorite (or granodiorite) field [70] and displays a subalkaline, medium-K calc-alkaline, and metaluminous character (Figure 6c,d). The DI ratio was 55.32. The Luxiping unit and Yingzizui unit exhibited high SiO$_2$ and Al composition, as well as low Fe, MgO, CaO, P$_2$O$_5$, and TiO$_2$ content and Mg$^{\#}$ ratios (Figure 5). The SiO$_2$ concentration spread from 67.60 wt.% to 75.47 wt.%, with an average of 71.33 wt.%, while Al$_2$O$_3$ varied between 13.78 wt.% and 16.54 wt.%, with an average of 15.30 wt.%. Combined, the K$_2$O + Na$_2$O contents ranged from 4.95 to 7.05 wt.%, averaging 6.25 wt.%, while the Na$_2$O/K$_2$O ratio varied between 1.74 and 9.10, with a mean of 3.51. The A/CNK ratio spanned 1.04–1.10, indicating a peraluminous, subalkaline, and medium-K calc-alkaline affinity (except for one sample that displayed a low-K calc-alkaline character) (Figure 6c). The DIs were 74.84 to 82.62, with an average of 79.30, and the Mg$^{\#}$ ratios were 13.25 to 33.91, with an average of 22.87. Overall, the rocks fell into the granodiorite–granite domains (Figure 6a,b) [70].

The late series were characterized by high SiO$_2$; low Fe, MgO, CaO, P$_2$O$_5$, and TiO$_2$ contents; and low Mg$^{\#}$ ratios. They displayed higher K$_2$O contents and DIs, yet lower Na$_2$O and CaO contents than the early series (Figure 5). The SiO$_2$ concentrations were 71.94 wt.% to 76.47 wt.%, with an average of 73.49 wt.%, while the Al$_2$O$_3$ contents were 12.79 wt.% to 14.92 wt.%, with an average of 14.10 wt.%. Combined, the K$_2$O + Na$_2$O concentrations were between 6.48 and 7.54 wt.%, with an average of 6.99 wt.%, and the Na$_2$O/K$_2$O ratios were 0.91 to 1.87, with a mean of 1.38. The A/CNK ratios showed a spread of 1.06–1.10, which is suggestive of peraluminous composition, and they further displayed a subalkaline and medium-to-high-K calc-alkaline association (Figure 6c). The

DIs were 81.30 to 90.89, with an average of 85.06. The Mg$^{\#}$ ratios were between 11.92 and 22.66, with an average value of 18.77. They fell into the granite domains (Figure 6a,b) [70].
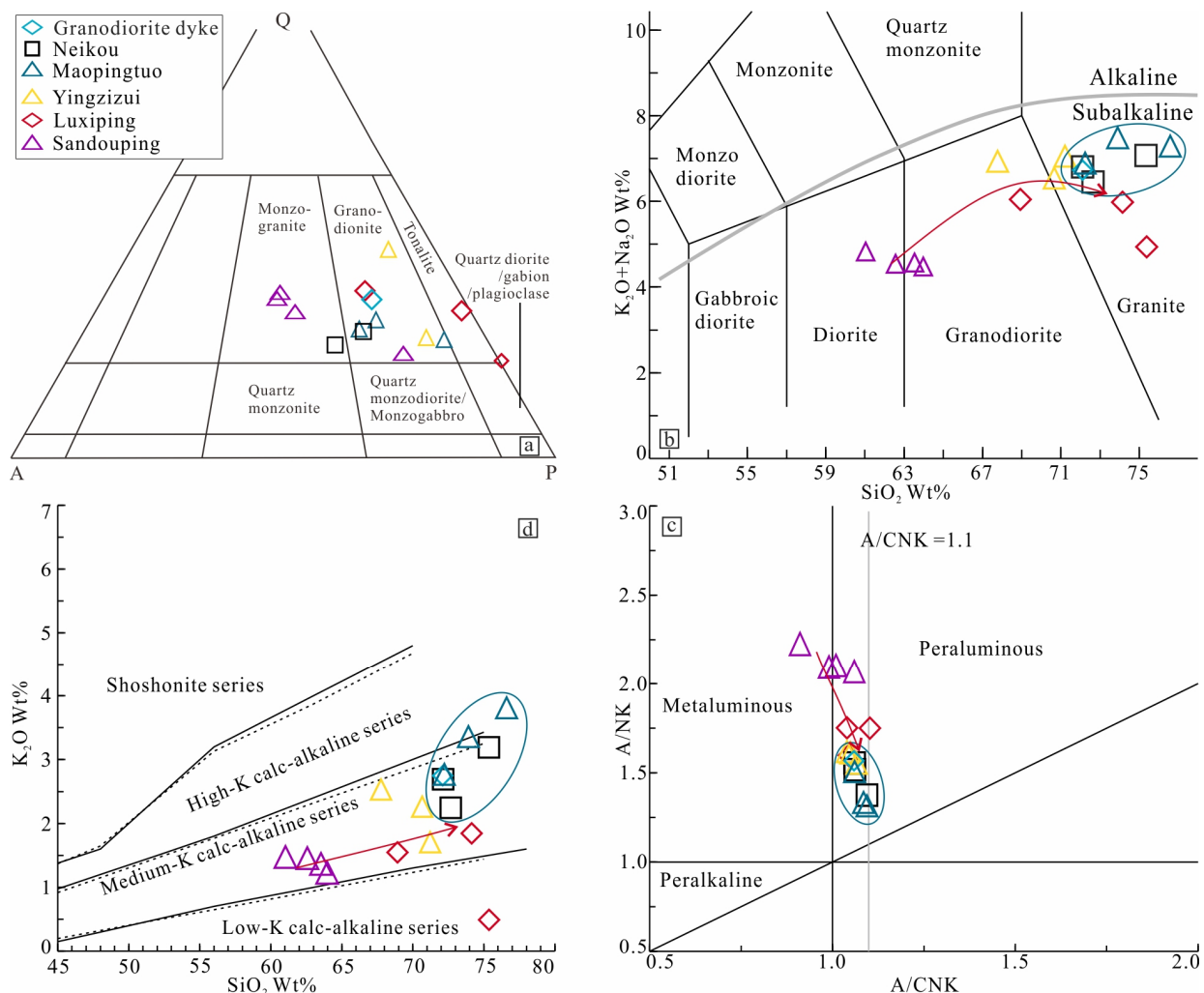

Figure 6. Geochemical discriminations for the Hbl-rich diorite and monzogranite. (**a**) Q A-P (after Streckeisen [71]), (**b**) Na$_2$O + K$_2$O-SiO$_2$ (after Le Maitre, Streckeisen [72]), (**c**) K$_2$O-SiO$_2$ (after Peccerillo and Taylor [73]), (**d**) A/NK-A/CNK (after Maniar and Piccoli [74]). A/NK = Al$_2$O$_3$/(Na$_2$O + K$_2$O) (mol), A/CNK = Al$_2$O$_3$/(CaO + Na$_2$O + K$_2$O) (mol). The red lines display the relations of the early series for the Huanglingmiao granitic complex.

4.2.2. Rare Earth Elements

For the early series, an obvious differentiation of light rare earth elements (LREEs) with heavy rare earth elements (HREEs) was displayed. The Sandouping unit had a total rare earth element (REE) content of 251.68 ppm (Table S4). The LREE/HREE, La$_N$/Yb$_N$, and Sm/Nd ratios were 15.27, 21.96, and 0.69, and the corresponding δEu and δCe ratios were 0.77 and 1.06, respectively (Figure 7a). The Luxiping and Yingzizui units exhibited a variable total REE composition of 41.29 ppm to 113.48 ppm, with an average value of 73.56 ppm (Table S4). The high LREE/HREE ratios were 6.18 to 20.48, and the corresponding La$_N$/Yb$_N$, Sm/Nd, δEu, and δCe ratios were 4.60–31.63, 0.14–0.23, 1.05–1.86, and 0.92–1.20, respectively. These lithologies expressed a slightly positive Eu anomaly (Figure 7a). The Luxiping unit was marked by lower total REE contents and more variable LREE/HREE and La$_N$/Yb$_N$ ratios than the Yingzizui unit.
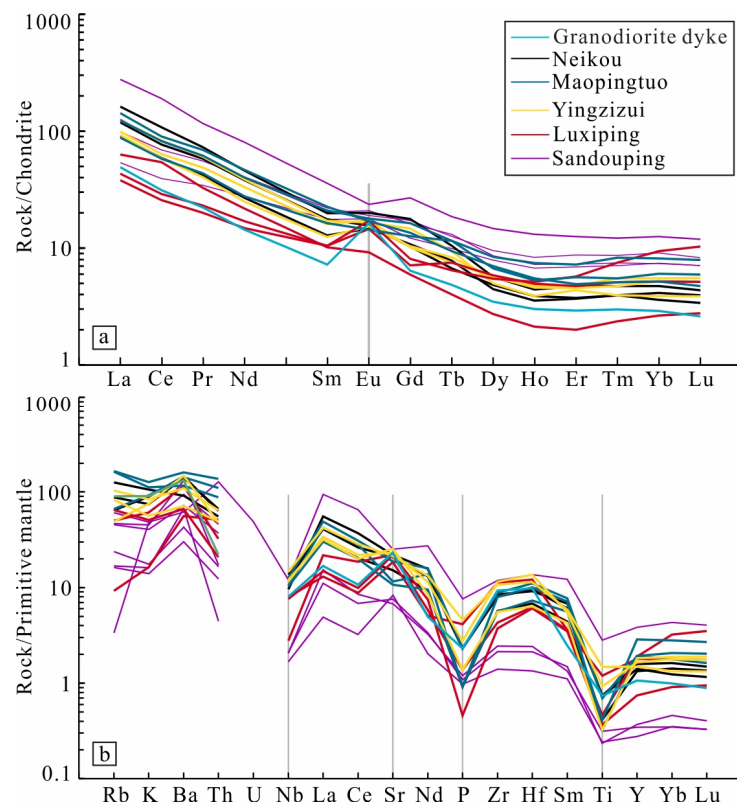
Figure 7. (**a**) Chondrite-normalized REE distribution patterns for the Huanglingmiao granitic complex and (**b**) primitive mantle-normalized trace elements for the Huanglingmiao granitic complex. The chondrite-normalized values and mantle values are from Sun and McDonough [75].

For the late series, the total REE contents were distributed between 45.09 ppm and 143.49 ppm, with an average value of 100.86 ppm (Table S4). Differentiation of the LREEs relative to the HREEs was discernible, and they were marked by high LREE/HREE ratios that spread from 8.95 to 19.42. The associated La_N/Yb_N, Sm/Nd, δEu, and δCe ratios were 10.76–34.16, 0.14–0.19, 0.97–2.39, and 0.91–0.99, respectively. The granodiorite dyke contained lower total REE content, higher δEu, and a slightly positive Eu anomaly than the Maopingtuo and Neikou units (Figure 7a).

4.2.3. Trace Elements

The trace-element data shown in Table S4 were broadly similar across the series (Figure 7b). However, the Sandouping unit typically contained a higher trace-element content than the late series. It displayed enrichment in large-ion lithophile elements (LILEs, i.e., Ba and Sr) and high field-strength elements (HFSEs, i.e., Th, Zr, and Hf) and depletion in some HFSEs (Nb, Ta, Ti, and P). The Luxiping and Yingzizui units equally recorded enrichment in LILEs (i.e., K, Ba, and Sr) and HFSEs (i.e., Th, Zr, and Hf), as well as depletion in other HFSEs (i.e., Nb, Ta, Ti, and P), and the Maopingtuo and the Neikou units recorded slight positive abnormalities in LILEs (i.e., K and Ba) but were depleted in HFSEs (i.e., Nb, Ti, and P). However, the granodiorite dyke exhibited the same trace-element distribution pattern as the Luxiping and Yingzizui units.

4.3. Zircon Lu-Hf Isotopes

The zircon Lu-Hf isotopic results for the HGC listed in Table S5 show different peaks and ranges of Hf isotopes for the two rock-series types. From the early to the later intrusions, the ratios of εHf (t) decreased and the model ages increased (Figure 8). The Sandouping unit exhibited similar T_{DM2}, younger T_{DM1}, and higher $\varepsilon_{Hf}(t)$ for the Luxiping and Yingzizui units, and the Yingzizui unit displayed varied isotopic contents. The Neikou unit was

divided into two groups (i.e., Group #1 and Group #2), with Group #1 representing the magmatic evolution event that formed the Neikou unit. Group #1 values were suggested to be similar to the late-series lithologies and Group #2 with the Luxiping and Yingzizui units, all being lower than those of the upper crust [76].

The 16 spots tested for the Lu-Hf isotopes for the Sandouping unit (Sample D110) contained $^{176}Hf/^{177}Hf$ and $^{176}Lu/^{177}Hf$ ratios between 0.281970 and 0.282240 and 0.000433 and 0.001119, respectively. The T_{DM1} ranged from 1415 to 1793 Ma, with a mean of 1663 Ma, and the T_{DM2} ranged from 1760 to 2350 Ma, with an average of 2144 Ma. Their $\varepsilon_{Hf}(t)$ values spread from −9.7 to −0.5 and had a mean of −6.3 (Figure 8).
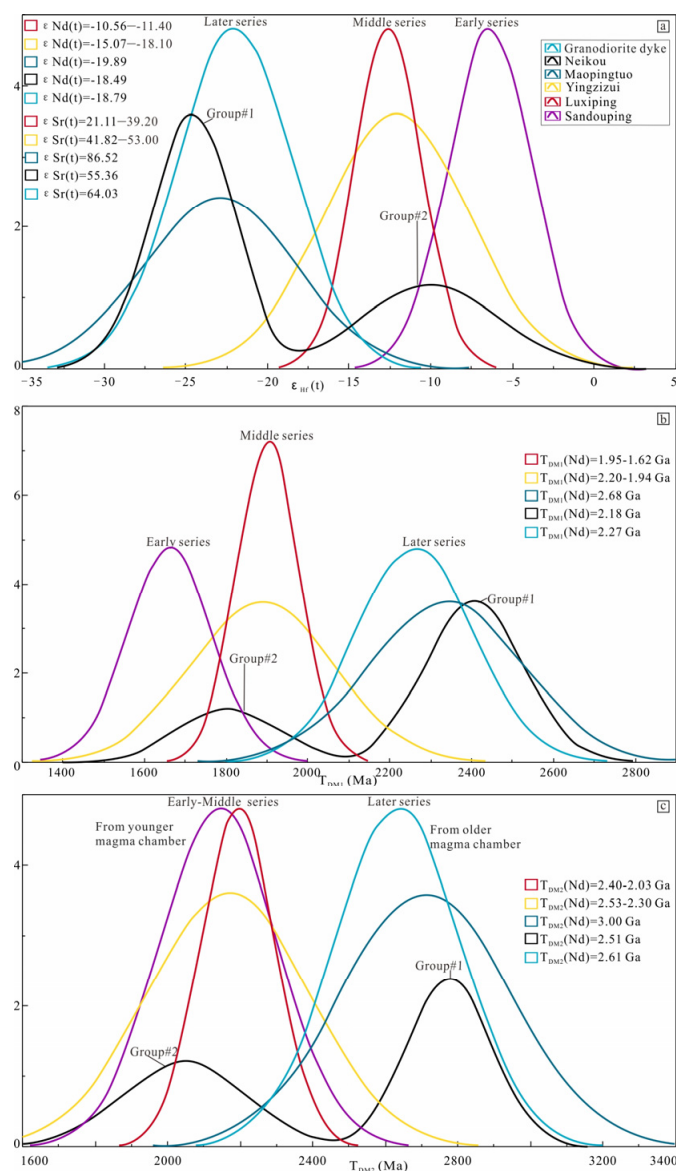

Figure 8. The Lu-Hf isotope data plotted on a histogram. (**a**) Histogram for $\varepsilon_{Hf}(t)$, (**b**) histogram for T_{DM1}, and (**c**) histogram for T_{DM2}.

The 16 spots analyzed for the Lu-Hf isotopes from the Luxiping unit (Sample PM054–12–1) possessed $^{176}Hf/^{177}Hf$ and $^{176}Lu/^{177}Hf$ ratios of 0.281809–0.282030 and 0.000634–0.001814, respectively. The T_{DM1} estimates of 1739–2006 Ma had a mean of 2194 Ma, while their corresponding T_{DM2} values were 1979–2338 Ma and had an average of 1902 Ma. Associated $\varepsilon_{Hf}(t)$ estimates of −15.2 to −8.3 produced a mean of −12.6 (Figure 8).

The 14 spots sampled for the Lu-Hf isotopes from the Yingzizui unit (Sample PM053–31–1) displayed $^{176}Hf/^{177}Hf$ and $^{176}Lu/^{177}Hf$ ratios spanning 0.281372–0.282146 and

0.001040–0.002318, respectively. Their corresponding T_{DM1} values were 1614–2655 Ma and had an average of 1954 Ma, the T_{DM2} values had an average of 2249 Ma with values ranging from 1797 to 3132 Ma. Estimated $\varepsilon_{Hf}(t)$ values of −31.0 to −4.7 average −13.7 (Figure 8).

The 18 spots tested for Lu-Hf isotopes for Maopingtuo unit (Sample PM056–39–1), contained two ancient zircons spots that showed different isotopic compositions indicating an allogenous origin. The $^{176}Hf/^{177}Hf$ and $^{176}Lu/^{177}Hf$ ratios of the remaining 16 spots fluctuated between 0.281368 and 0.281805 and 0.000997 and 0.003472, respectively. Their associated T_{DM1} values of 2099–2769 Ma average 2338 Ma, with T_{DM2} estimates of 2405–3185 Ma having a mean of 2713 Ma. The corresponding $\varepsilon_{Hf}(t)$ values of −32.4 to −17.1 average −23.1 (Figure 8).

A total of 14 spots analyzed for Lu-Hf isotopes for the Neikou unit (Sample PM056–12–1), contained a single ancient zircon characterized by a different isotopic composition (Table S5). The rest of the 13 spots were divided into group#1 and group#2, with group#1 distinguished by $^{176}Hf/^{177}Hf$ and $^{176}Lu/^{177}Hf$ ratios of 0.281491–0.281676 and 0.001791–0.003252, respectively. The T_{DM1} values of 2222–2537 Ma had a mean of 2406 Ma and a T_{DM2} of 2612–2236 Ma with an average of 2777 Ma. The corresponding $\varepsilon_{Hf}(t)$ measurements of −28.6 to −20.7 had a mean of −24.6. The group#2 measurements for $^{176}Hf/^{177}Hf$ and $^{176}Lu/^{177}Hf$ ratios spread between 0.281906 and 0.282155 and 0.000997 and 0.003472, respectively. They had related T_{DM1} values of 1643–1941 Ma with an average of 1809 Ma and T_{DM2} values of 1819–3185 Ma, with a mean of 2047 Ma. Their $\varepsilon_{Hf}(t)$ values ranged between −14.8 and −4.9, with an average of −10 (Figure 8). Combined with the U-Pb data, the Group #1 results include the source rock age and Lu-Hf isotope of the Neikou unit.

For the 11 spots tested for the Lu-Hf isotopes from the granodiorite dyke (Sample D3336–1), one spot was identified as representing an ancient zircon (Table S5). The other 10 spots were characterized by $^{176}Hf/^{177}Hf$ and $^{176}Lu/^{177}Hf$ ratios distributed between 0.281549 and 0.281918 and 0.001018 and 0.002839, respectively. The related T_{DM1} values were 1919–2502 Ma and had an average of 2262 Ma; the T_{DM2} recorded values of 2196–2870 Ma and had a mean of 2635 Ma; and the $\varepsilon_{Hf}(t)$ values were −43.2 to −30.2 and had an average of −39.0 (Figure 8).

4.4. Whole-Rock Sr-Nd Isotopes

Table S6 gives the whole-rock Sr–Nd isotope data and the calculated initial isotopic ratios for the representative samples from the HGC. These include two samples each from the Luxiping (PM054–12–1 and PM050–31–1) and Yingzizui (PM053–31–1 and PM050–46–1) units, as well as one from the Maopingtuo (PM056–39–1) unit, Neikou (PM050–54–1) unit, and the granodiorite dyke (D3336–1), respectively. These values fell within the south China craton lower-crust field [77]. The late-series rocks were markedly distinguished by lower εSr and higher εNd values compared to the early-series lithologies. Further, the εNd and Nd model ages were coincident with the zircon Hf isotope values (Figure 8).

For the Luxiping unit, the $^{87}Sr/^{86}Sr$, εSr, $^{143}Nd/^{144}Nd$, and εNd ratios spanned 0.70956–0.70559, 21.11–39.20, 0.511504–0.511604, and −10.56−−11.40, respectively. Their associated T_{DM1} and T_{DM2} Nd model ages ranged from 1.62 to 1.95 Ga and 2.03 to 2.40 Ga, respectively. In the case of the Yingzizui unit, the $^{87}Sr/^{86}Sr$, εSr, $^{143}Nd/^{144}Nd$, and εNd ratios bracket had values of 0.71034– 0.71097, 41.82–53.00, 0.51114–0.51127, and −15.07−−18.10, respectively, with corresponding T_{DM1} and T_{DM2} Nd model ages of 1.94–2.20 Ga and 2.30–2.50 Ga, respectively. The Maopingtuo unit produced $^{87}Sr/^{86}Sr$, εSr, $^{143}Nd/^{144}Nd$, and εNd ratios of 0.72248, 86.52, 0.511157, and −19.89, respectively, as well as a T_{DM1} and T_{DM2} Nd model age of 2.68 Ga and 3.00 Ga, respectively. The Neikou unit on their part displayed $^{87}Sr/^{86}Sr$, εSr, $^{143}Nd/^{144}Nd$, and εNd ratios of 0.71176, 55.36, 0.51111, and −18.49, respectively, with T_{DM1} and T_{DM2} Nd model ages of 2.18 Ga and 2.51 Ga, respectively. On the other hand, $^{87}Sr/^{86}Sr$, εSr, $^{143}Nd/^{144}Nd$, and εNd ratios for the granodiorite dyke corresponded to 0.71149, 64.03, 0.511162, and −18.79, respectively, with T_{DM1} and T_{DM2} Nd model ages of 2.27 Ga and 2.61 Ga, respectively.

5. Discussion

5.1. Two-Stage Petrogenesis of the HGC

The HGC was formed by multiple stages of magmatic intrusions [38,48] and contains various rock types [49]. Previous studies have produced different classification schemes for various rock types and their distribution due to the use of different classification schemes and insufficient geochemical data; meanwhile, the major lithology of the HGC remains ambiguous. The recent geologic investigation associate the major lithology of the HGC to a set of porphyric biotite plagioclase granite. Ma, Li [53] previously classified the HGC as a set of porphyric trondhjemite, and this was later corrected to a set of porphyric biotite granodiorite [49]. Nonetheless, most researchers still believe the major lithology of the HGC to be trondhjemite, with a few tonalite and granodiorite bodies [6,16,50–52]. Based on a large-scale geologic investigation and systematic classification of rock types, the major rock types were found to be the Neikou medium-grained porphyric granodiorite, followed by the Maopingtuo oligoporphyric granodiorite and the Yingzizui granodiorite, in the margin of the HGC (Figure 2). The Sandouping tonalite and the Luxiping trondhjemite only exhibited small bodies of the HGC at the peripheral margin of the latter. The granodiorite dykes were widely presented yet the volumes were small. Combining the field characteristics with mineral and geochemical contents [70,78], we believe that the major lithology of the HGC is granodiorite, with a small fraction of tonalite, trondhjemite, and granodiorite.

Previous studies using different methods to evaluate the formation age of the HGC acquired a granite formation age of 839 and 800 Ma [26,27,53]. Our data suggest that this systematic error is the result of the use of different analytical methods and rock classifications schemes, leading to a lack of consensus. To bypass this shortcoming of previous studies, we selected a complete lithological section to test the geochronological data of the HGC based on the sequence of rock intrusion patterns and the relationships captured by them—i.e., from the early-to-late-stage Sandouping, Luxiping, Yingzizui, Maopingtuo, and Neikou units, as well as the granodiorite dyke (Figures 2 and 3). For example, geochemically, 60.69 wt.% SiO_2 and 25 wt.% quartz makes up the Sandouping unit. The Luxiping and Yingzizui units, on the other hand, are composed of a smaller hornblende fraction and higher quartz and SiO_2 compositions than the Sandouping unit, while the mineral textures of the late-series assemblages are clearly different from the early series (Figures 3 and 4). The late-series samples contained a high quartz and SiO_2 content (Figure 3). The increasing quartz content (i.e., silicon concentration) and decreasing hornblende composition also exhibited a distinct trend with the early series (Figures 3 and 4). Moreover, the Hf and Sr-Nd isotope composition of the early- and late-series rocks were dissimilar (Figure 8). In addition, the oligoporphyritic and porphyric textures characterized the Maopingtuo and Neikou units, respectively (Figure 3).

The present evidence shows that the Sandouping tonalite intruded on the Duanfangxi appinite suite and that the latter was, in turn, intruded on by the Luxiping and Yingzizui units (Figure 2). Unpublished age constraints suggest that the Duanfangxi appinite suite formed before ca. 870 Ma, while the after ca. 870 Ma formation age of the Sandouping unit was found to be consistent with our inferred zircon age of 865 Ma. Thus, we believe the Sandouping unit represents the early stage of the HGC that was generated at ca. 865 Ma. The Luxiping trondhjemite intruded on the Jingpansi tonalite, the Mesoproterozoic metamorphic strata, and the basic–ultrabasic rocks (Figure 2), which together are covered by the Nanhua formation. The Luxiping trondhjemite was observed to always capture the Jingpansi tonalite and the Sandouping trondhjemite enclaves [25,27,48], whose appinite-like composition indicates a relation to the Duanfangxi appinite suite. A formation of the Sandouping tonalite between 863 ± 9 and 855 ± 10 Ma [25,27] indeed suggests an age older than 839 ± 17 Ma, which was inferred from the trondhjemite in the Nanhua formation cover [27]. The Yingzizui granodiorite, distributed as an annular ring between the Luxiping trondhjemite and the Maopingtuo oligoporphyritic granodiorite, first intruded into the Luxiping trondhjemite. This event was succeeded by subsequent intrusions into the Luxiping trondhjemite by the Maopingtuo oligoporphyritic granodiorite (Figure 2).

This is consistent with the older 852 Ma formation age of the Luxiping unit compared to the 850 Ma for the Yingzizui unit (Figure 4). We propose that the early-series rocks of the HGC formed at ca. 865–850 Ma.

Next, we inferred that the Maopingtuo oligoporphyritic granodiorite intruded into the Yingzizui unit and was then later intruded into by the Neikou porphyric granodiorite. The Neikou unit that surge-intruded into the Maopingtuo unit (Figure 2) contains enclaves of biotite schist, dioritic porphyrite, and porphyric biotite–quartz diorite. These results indicate that the Neikou unit formed much later than the Maopingtuo unit. In support of this proposition, our zircon ages suggest that the Maopingtuo unit formed at ca. 844 Ma and the younger Neikou unit by ca. 825 Ma. The intrusion of other rocks by the granodiorite dyke point to their generation at a later stage compared to the Neikou unit with its corresponding zircon formation age of ca. 797 Ma. These geochemical results were similar to those obtained for the Maopingtuo and Neikou units. Thus, we believe these two lithologically series contain the late-series rocks of the HGC that has formed since ca. 844 Ma.

5.2. Magmatic Source and Evolution of the HGC

The low Mg# ratios (with a single result from the Sandouping unit being >45) and the isotopic results indicate that the HGC could not have originated from the mantle (Figures 5f, 9 and 10). The HGC is characterized by rare Al-rich minerals, inherited zircons, low A/CNK ratios (most values being <1.10), and high LREE concentrations. Combined with the concentration of various other elements, they indicate that the HGC is different from the normal S-type granites formed by partial melting of upper crustal sediments. Biotite is enriched in the HGC and hornblende in the Sandouping unit, representing a hydro-rich magma source. The geochemical results exhibit low K and middle alkaline contents. Combined with their elemental composition, the HGC is suggested as not belonging to the A-type granites that are typically composed of an anhydrous and a high K content. All of them have low A/CNK ratios, high LREE concentrations, and no enrichment in HREEs, indicating the HGC is affiliated with middle-K calc-alkaline I-type granite-like rocks (Figures 6 and 11; Skjerlie and Johnston [79], Douce [80]).

The calc-alkaline I-type granites could have been generated by three primary petrological processes [81–84]: (1) early fractional crystallization and cumulation derived from cogenetic magmas [85,86]; (2) partial melting of metaigneous rocks [87]; and (3) a mixing of crust- and mantle-derived magmas [88,89]. The late series were rich in felsic minerals (Figure 3), with the whole-rock major geochemical results being characterized by high SiO_2 (except for the Sandouping unit) content; low Fe, MgO, and TiO_2 contents; and low $Mg^{\#}$ ratios—with the exception of the $Mg^{\#}$ ratio of the Sandouping unit that was >45 (Figure 5). The REE-trace geochemical results containing high La contents of LREE/HREE, Th/La, and La/Yb ratios (Figures 7 and 12) point to a crustal origin [90,91], which is consistent with the zircon Hf and whole-rock Sr-Nd isotopic analyses (Figures 9 and 10). These observations suggest that the HGC could not have been generated by the early fractional crystallization and cumulation from cogenetic magmas, with partial melting of metaigneous rocks being the major source.
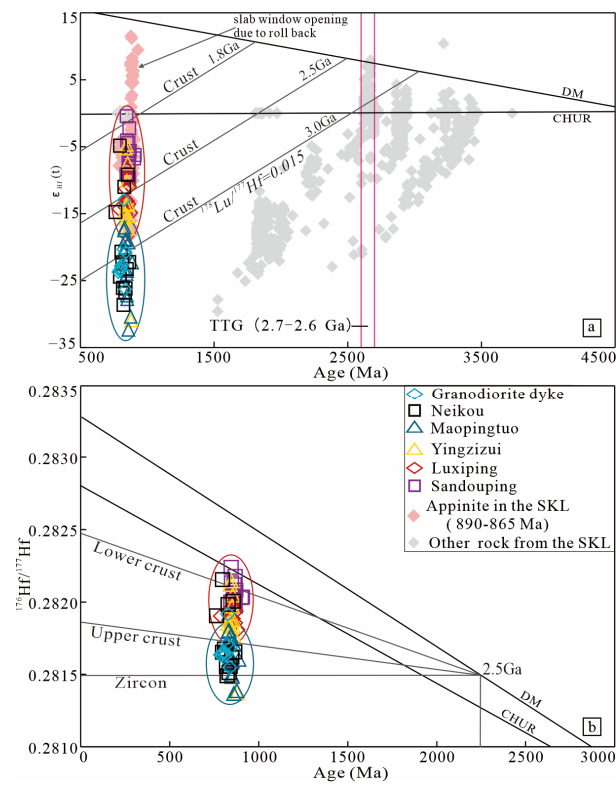
Figure 9. Hf isotope evolution diagram. (**a**) $\varepsilon_{Hf}(t)$-zircon age and (**b**) $^{176}Hf/^{176}Hf$-zircon age. Data sources: Peng, Wu [22], Zhao, Zhou [26], Zhao, Zhou [27], Gao, Ling [35], Gao, Yang [36], Guo, Gao [37], Li, Zhou [39], Qiu, Ling [58], Xiong, Zheng [92], Chen, Gao [93], Guo, Zheng [94], Guo, Zheng [95], Wei, Zhou [96], Zhang, Zheng [97].
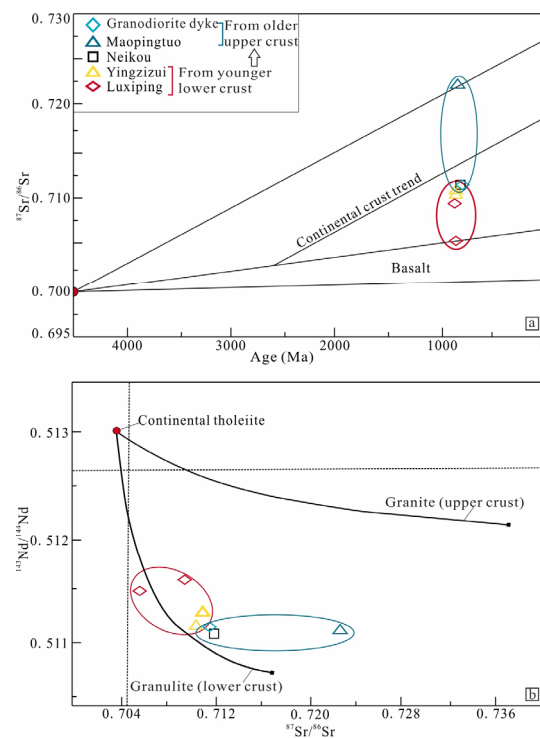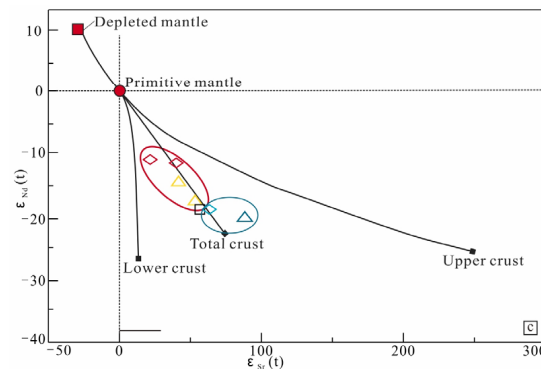

Figure 10. *Cont.*

Figure 10. Sr-Nd isotopic Harker diagrams of the HGC. (**a**) $^{87}Sr/^{86}Sr$-zircon age, (**b**) $^{143}Nd/^{144}Nd$-$^{87}Sr/^{86}Sr$, and (**c**) $\varepsilon_{Nd}(t)$-$\varepsilon_{Sr}(t)$.
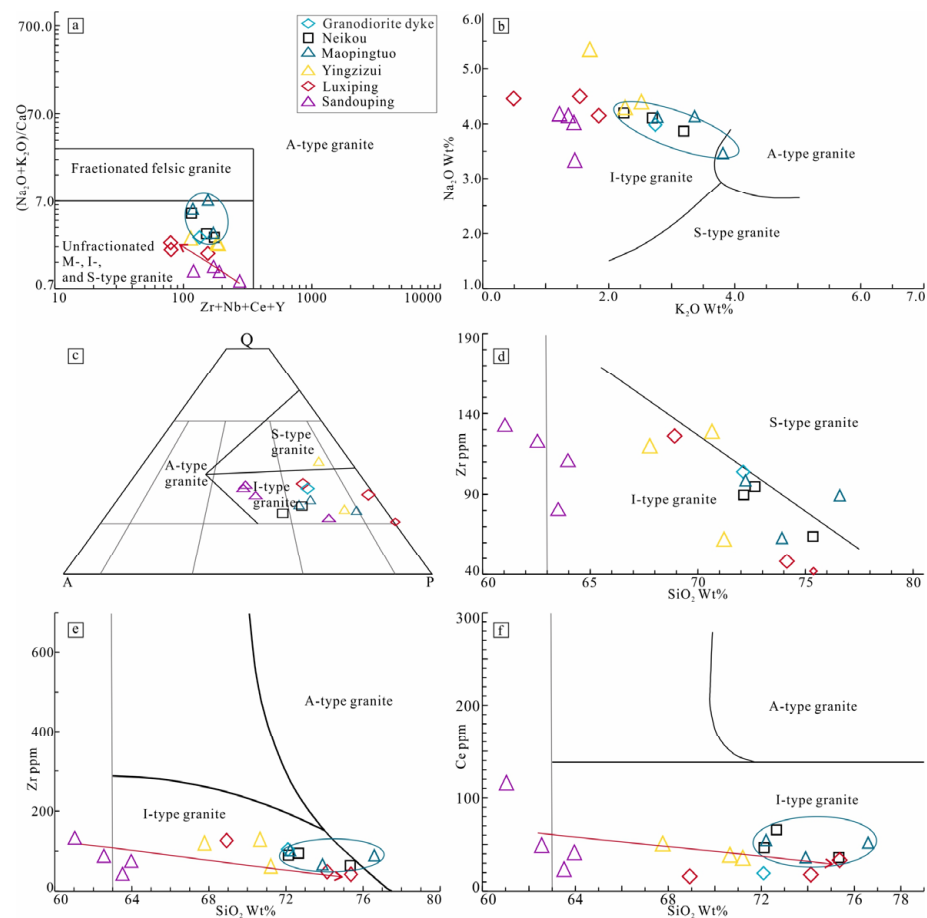
Figure 11. Discrimination diagrams for granite rock types. (**a**) $K_2O + Na_2O/CaO$-Zr + Nb + Ce + Y (after Whalen, Currie [31]); (**b**) Na_2O-K_2O; (**c**) Q-A-P diagram (after Lameyre and Bowden [98]); (**d**) Zr-SiO_2; (**e**) Zr-SiO_2; and (**f**) Ce-SiO_2 (**b**, **e**, and **f** after Collins, Beams [99]). The red lines display the relations of the early series for the Huanglingmiao granitic complex.

There are varied dioritic (appinite-type rock) and mafic enclaves in the HGC. The Nb/Ta ratio ranged from 4.5 to 21.96, with an average of 14.33, and most values were lower than the original mantle composition of 17.5 and greater than the average continental crust value of 11 [100,101]. The La/Nb ratio ranged from 1.58 to 7.54, with an average of 3.57, and this was greater than the original mantle value of 0.94, albeit a few less than the average crustal value of 2.2, which together indicate their major crustal origin [102]. The I_{Sr} of the early-series and late-series rocks of 0.70471–0.7096 showed slight variation but remained

close to the composition of their upper mantle crustal source of 0.702–0.706. In particular, the 45.89 $Mg^{\#}$ ratios of the Sandouping unit being >45 [103], with associated $^{176}Hf/^{177}Hf$ ratios of 0.281970–0.282240, are reminiscent of a typical mixing composition [104]. The similar T_{DM2} values for the early series, and yet different $\varepsilon_{Hf}(t)$ values, indicate a decoupling of the Hf isotope distribution due to the addition of heterologous magma. Collectively, the results indicate a strong effect of mantle-derived magma on the generation of the early-series rocks.
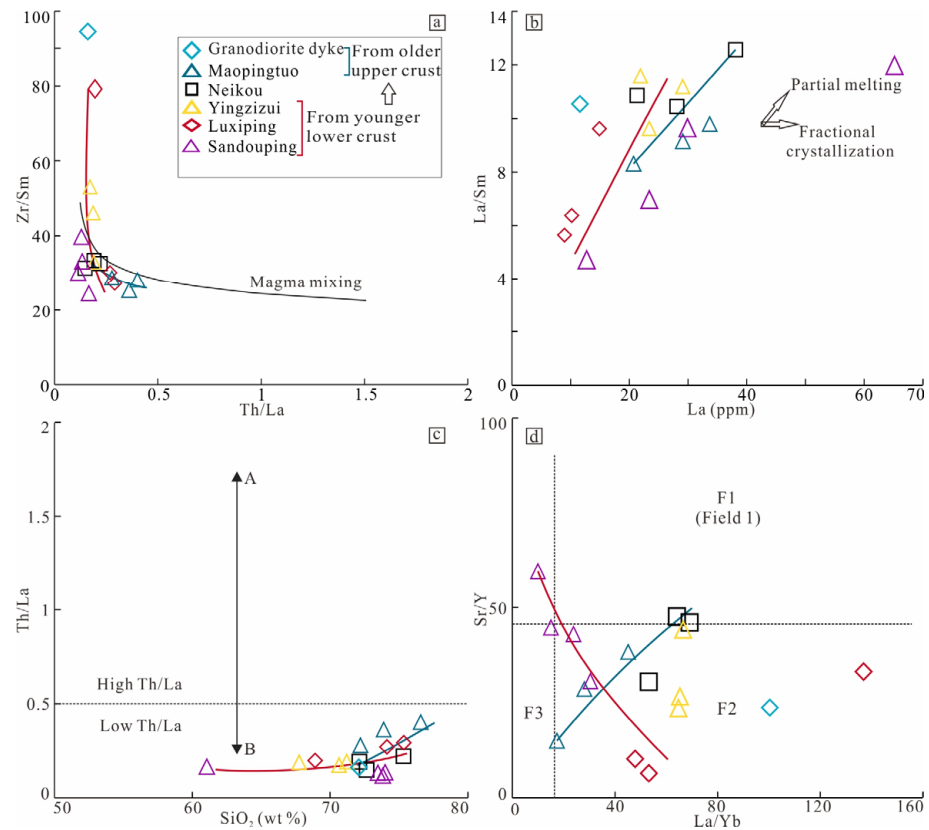
Figure 12. The genetic types and evolution relationships of the Huanglingmiao granitic complex. (**a**) Zr/Sm-Th/La. (**b**) La/Sm-La. (**c**) Th/La-SiO$_2$. High Th/La ratios in the magmatic rocks indicate relatively large contributions from sedimentary source rocks. 'A' indicates a partial melting of sediment-dominated crustal sources and 'B' indicates a partial melting of mafic crustal sources. (**d**) Sr/Y-La/Yb. F1 indicates the adakitic melts derived from eclogitic rocks in the garnet stability field with little or no plagioclase. F2 indicates the crustal melts in the stability field for both plagioclase and garnet. F3 indicates the crustal melts in the stability field for plagioclase with little or no garnet present. (**a,b**) After Du, Long [105]; (**c,d**) after Wang, Xue [106]. The red (later series) and blue (early series) lines display the evolution relations of the different series for the Huanglingmiao granitic complex.

Several lines of evidence suggest that the crustal texture and mantle magmatic intensity together dominate the complexity of the source materials that formed the HGC. Thus, the sources of the HGC may be from deep sources. Previous studies have indicated that tonalite–dioritic, trondhjemitic, and granodioritic gneiss (TTG gneiss); little residual amphibolite rock; and young mafic rock compose the major body of the deep crust in the YC northern margin [36,37,94,95]. It has also been suggested their low Sr contents and Sr/Y ratios rule out amphibolite rocks as a major source of the HGC, while some studies point to TTG gneiss as the protolith of the asynchronous granites in the KL area [22,39,52,92]. Moreover, because several rocks of mantle origin, since the early Neoproterozoic, were found to be associated with active mantle magmatic events and the HGC [18,19,21,23,24],

we consciously discussed the locations and nature of the partial melting and mantle effects on the generation of the HGC.

Zircon Hf isotope distribution serves as a useful tool for tracing the magmatic source and elucidating the interactions between the crust and mantle [104,107,108]. Accordingly, the Hf isotopes indicate primary magma chamber fractionation for the Sandouping unit after 2.5 Ga, which produced $^{176}Hf/^{177}Hf$ ratios similar to the lower crust values and are characterized by magmatic mixing. Together with a high hornblende, Fe, and MgO content, and high $Mg^{\#}$ ratio (Figures 4 and 5), the Yingzizui and Luxiping units exhibited rare hornblende, low Fe, and MgO concentrations, as well as low $Mg^{\#}$ ratios (Figures 4 and 5). Their associated Hf isotopes indicated primary magma chamber fractionation after 3.0 Ga, and they were affected by 2.7–2.6 Ga TTG gneiss (Figure 9). The distribution of $^{176}Hf/^{177}Hf$ ratios between the upper and lower crust and their general closeness to lower crust values, together with the Hf isotope distribution being consistent with Sr-Nd isotopes (Figure 10), indicate a generation of the early-series rocks being mainly from the lower crustal rocks mixed with mantle materials (Figures 9 and 13). For the late series, the Hf isotopes indicate that the primary magma chamber began fractionation before 3.0 Ga, and they also show a strong relationship of >2.9 Ga TTG gneiss (Figure 9) while their $^{176}Hf/^{177}Hf$ ratios are lower than those for the upper crust, with corresponding Hf isotopic results being consistent with their Sr-Nd isotope distribution (Figure 10). These observations point to the generation of the late series from shallower crustal TTG genesis (Figures 9 and 13).
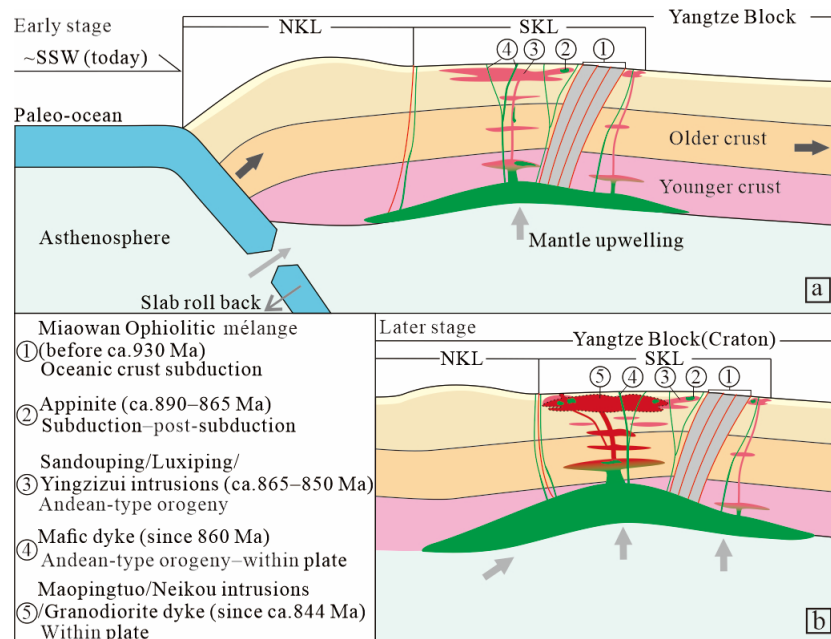

Figure 13. Schematic diagrams showing the tectonic processes of the Kongling terrane (no scale). (**a**) Early stage involving a partial melting of the lower crust. (**b**) Late stage involving a partial melting of the upper crust.

For the early intrusions, the grain size transitioned from fine- and medium-grained rocks. In particular, some granodioritic dykes generated at the late stage. There was a significantly positive correlation between the SiO_2 with the alkaline and DI ratios, and yet the negative correlations between the SiO_2 with the Fe, MgO, CaO, and P_2O_5 concentrations, and $Mg^{\#}$ ratios (Figures 5 and 6) showed a TTG-like evolutional sequence of early series. The late series displayed different characters. The appinite suite discovered in the KL area indicate that the slab window was opened, resulting in oceanic slab roll back and mantle upwelling at the continental margin since ca. 890 Ma [109].

This mantle upwelling controls the generation of the early chamber in the deep crust, leading to the magma mixing. With the depletion of crustal materials by partial melting, the chamber location has migrated from deeper depths toward a shallower surface (Figure 13). Thus, there are different sources of the HCG.

5.3. Petrogenetic Setting of the HGC

Most of the HGC displays an I-type granite character. However, constraining the geodynamic setting of I-type granites is complex because of their occurrence in active continental margins and post-collisional extensional environments [47,110,111]. Due to this petrogenetic setting complexity of I-type granites, some scholars believe that the HGC was generated in a magmatic arc environment [48,54]; yet, most believe the HGC to be related to the mantle plume activity in South China that represents a extensional environment [6,50,52,55,56]. Thus, systematically investigating the complex tectonic evolution of the KL terrane, combined with the geochemical characteristics and affinities of the HGC, is necessary to gain greater insights into the petrogenetic setting of the HGC. The SSZ-type ophiolitic mélange and Late Magmatic Suite from the Miaowan area recorded subduction-related magmatic activities before 900 Ma [19,23] in the KL terrane, which is on the northern margin of the YC. Moreover, the recent documentation of the appinite suite in the SKL area provide further evidence for the subduction activities ending before ca. 870 Ma. Some scholars believe that the ca. 860 Ma Miaowan mafic dykes, which are contemporaneous olivine–gabbroic rocks, and 850 Ma diorite–granite record the post-collisional activity in the KL terrane [20,21,24,27,52,97,112]. Thus, most scholars believe that the HGC was generated in a post-collisional environment [6,50,52,55,56].

However, a petrogenetic investigation of the HGC indicated that the depositional setting was not a continuum of the post-collisional environment activity. The SiO_2 contents and $^T FeO^*/MgO$ and K_2O/Na_2O ratios of 60.69–75.47 wt.% and 2.10–13.17, respectively, are consistent with the results of Jakeš and White [113] and have an active continental margin setting that is characterized by 56–75 wt.% SiO_2 and $FeO^*/MgO > 2.0$. The significant calc-alkaline character of the lithologies, including Nb and Ta negative anomalies, as well as the enrichment of LILEs and LREEs, indicate the HGC formed in arc-related environment [29,101,114]. Combined with existing Neoproterozoic magmatic–tectonic records in the northern margin of the YC, we believe the HGC was generated in an active continental margin environment. For the late series, we found a generous capture of zircons, higher K_2O content, and $\varepsilon_{Sr}(t)$ (Figure 6); yet, we also found lower $\varepsilon_{Hf}(t)$ and $\varepsilon_{Nd}(t)$ values in the early-series rocks (Figures 6 and 7). This indicates the sources were exchanged during the dynamic transition. From the early- to late-series lithologies, the geochemical contents displayed a trend from I-type granite to S/A-type granite (Figure 11), indicating that the late-series rocks were also influenced by within-plate magmatic activities.

5.4. Tectonic Importance

Cawood, Wang [1] reconstructed the ancient block that formed Nuna and Rodinia, leading them to suggest that the Yangtze and India blocks occupied a similar tectonic setting in the early Neoproterozoic. In line with this proposal, some studies have argued that Neoproterozoic granitoids and their associated basaltic magmas from northwestern India were formed in a continental arc environment, indicating there was an active Andean-type orogeny along this belt [115–117]. Further, the southwestern–western and northwestern–northern edges of the YC, which is composed by a series of late Mesoproterozoic-accreted arc terranes, contain subduction-related rocks that were formed before 900 Ma and granite-type rocks close to 800 Ma in age, with varied ages being inferred for the associated mafic dykes [24,97,118–121]. Here, we reconstructed a complete tectonic history for the KL terrane, combined with previously reported observations, to suggest an Andean-type orogeny of the within-plate extension for the HGC. The complete rock series recorded a sequential partial melting granitic rock process [34], during which the crust materials were consumed and the magma chamber upwelled toward the surface, similar to Himalayan-

type orogenic belt activity [122]. This led us to propose that the early arc-related series rocks indicate the existences of an Andean-type orogeny in the northern margin of the YC since ca. 865 Ma [27,48]. The within-continental feature of the late-series rocks point to a stable–extensional setting in the northern margin of the YC since ca. 845 Ma. This records a tectonic transition that is consistent with the absence of collisional orogeny in the margin of the YC [16,18–20,23–27,38,48,49]. Thus, we believe that the YC was formed by a series of Andean-type orogeny to within-plate activity events between ca. 865 and 800 Ma (Figure 13).

Recent studies have shown that the Rodinia supercontinent was mostly widely influenced by Grenville orogeny in the early Neoproterozoic [13,123], with most of the major continental blocks assembled into Rodinia through collisional orogeny between 1350 and 900 Ma [15,123–125]. However, reconstruction of the YC locates it at the northwest periphery of the Rodinia supercontinent [1–3,7,9–14], which is marked by the absence of collisional orogeny. Thus, the relationship of the YC to the Rodinia supercontinent is ambiguous. An increasing number of studies are beginning to show that the oceanic basin between the YC and the Cathaysian block (CB) may not have recorded the crucial subduction events controlled by the convergence of the Rodinia supercontinent, events which are otherwise recoded in the north–northwest margin [15,18,19,23,59,126–132]. In addition, the complete intermediate-acid rocks in the northern margin of the YC indicate the existence of tectonic processes that are characteristic of the Andean-type orogeny to within-plate activity (Figure 13). Combined with the occurrence of ophiolitic mélanges, appinite suites, and mafic dykes in this region [18,19,23,24,97,109,118–121], these observations indicate the presence of complete subduction to within-plate tectonic translation in the northern margin of the YC. This polar tectonic evolution is consistent with the oceanic–continental environment of the northern YC and the cratonization processed along with merging of the YC and CB. Importantly, this Andean-type orogeny to within-plate activity (ca. 865–797 Ma) perhaps promoted the convergence of the Yangtze craton to the Rodinia supercontinent—which is much later than those for the major active periods associated with the Grenville orogeny (ca. 1.0–0.8 Ga).

6. Conclusions

The Huanglingmiao granitic complex (HGC) is composed of early-stage tonalite, trondhjemite, and granodiorite, as well as late-stage oligoporphyritic granodiorite, porphyric granodiorite, and granodiorite dyke. The porphyric granodiorite forms the main body of the HGC. These five sets of rocks form at 865 ± 5 Ma, 852 ± 12 Ma, 850 ± 4 Ma, 844 ± 11 Ma, 825 ± 14 Ma, and 797 ± 8 Ma, respectively, and the generation of the HGC indicates there are multiple magma intrusive activities in the Kongling terrane in the Yangtze craton. The geochemical results indicate that the early-series rocks were generated from lower crustal mafic rock and were mixed with mantle materials, as well as that the late-series rocks originated from upper crustal TTG genesis. Combined with regional studies, it is suggested that the early-series rocks were generated in an active continental margin environment and that the late-series rocks exhibit a within-plate tectonic feature. Overall, the generation of the HGC point to its transition from an Andean-type orogeny to within-plate activity in the northern margin of the Yangtze craton represents the convergence of the Yangtze craton with the Rodinia supercontinent.

compositions of the zircons from the Huanglingmiao granitic complex;Table S6: The Sr–Nd isotopic compositions of the whole rock from the Huanglingmiao granitic complex.

References

1. Cawood, P.A.; Wang, W.; Zhao, T.Y.; Xu, Y.J.; Mulder, J.A.; Pisarevsky, S.A.; Zhang, L.M.; Gan, C.S.; He, H.Y.; Liu, H.C.; et al. Deconstructing South China and consequences for reconstructing Nuna and Rodinia. *Earth Sci. Rev.* **2020**, *204*, 24. [CrossRef]
2. Cawood, P.A.; Wang, Y.J.; Xu, Y.J.; Zhao, G.C. Locating South China in Rodinia and Gondwana: A fragment of greater India lithosphere? *Geology* **2013**, *41*, 903–906. [CrossRef]
3. Cawood, P.A.; Zhao, G.C.; Yao, J.L.; Wang, W.; Xu, Y.J.; Wang, Y.J. Reconstructing South China in Phanerozoic and Precambrian supercontinents. *Earth Sci. Rev.* **2018**, *186*, 173–194. [CrossRef]
4. Li, Z.X.; Bogdanova, S.V.; Collins, A.S.; Davidson, A.; De Waele, B.; Ernst, R.E.; Fitzsimons, I.C.W.; Fuck, R.A.; Gladkochub, D.P.; Jacobs, J.; et al. Assembly, configuration, and break-up history of Rodinia: A synthesis. *Precambrian Res.* **2008**, *160*, 179–210. [CrossRef]
5. Li, Z.X.; Li, X.H.; Li, W.X.; Ding, S.J. Was Cathaysia part of Proterozoic Laurentia? new data from Hainan Island, South China. *Terr. Nova* **2008**, *20*, 154–164. [CrossRef]
6. Li, Z.x.; Li, X.h.; Zhou, H.w.; Kinny, P.D. Grenvillian continental collision in south China: New SHRIMP U-Pb zircon results and implications for the configuration of Rodinia. *Geology* **2002**, *30*, 163–166. [CrossRef]
7. Shu, L.S. An analysis of principal features of tectonic evolution in South China Block. *Geol. Bull. China* **2012**, *31*, 1035–1053.
8. Shu, L.S.; Wang, J.Q.; Yao, J.L. Tectonic evolution of the eastern Jiangnan region, South China: New findings and implications on the assembly of the Rodinia supercontinent. *Precambrian Res.* **2019**, *322*, 42–65. [CrossRef]
9. Shu, L.S.; Yao, J.L.; Wang, B.; Faure, M.; Charvet, J.; Chen, Y. Neoproterozoic plate tectonic process and Phanerozoic geodynamic evolution of the South China Block. *Earth Sci. Rev.* **2021**, *216*, 30. [CrossRef]
10. Zhao, G.C.; Cawood, P.A. Tectonothermal evolution of the Mayuan assemblage in the Cathaysia Block: Implications for neoproterozoic collision-related assembly of the South China craton. *Am. J. Sci.* **1999**, *299*, 309–339. [CrossRef]
11. Zhao, G.C.; Cawood, P.A. Precambrian geology of China. *Precambrian Res.* **2012**, *222*, 13–54. [CrossRef]
12. Zhao, J.H.; Zhang, S.B.; Wang, X.L. Neoproterozoic geology and reconstruction of South China. *Precambrian Res.* **2018**, *309*, 1–5. [CrossRef]
13. Johansson, A.; Bingen, B.; Huhma, H.; Waight, T.; Vestergaard, R.; Soesoo, A.; Skridlaite, G.; Krzeminska, E.; Shumlyanskyy, L.; Holland, M.E. A geochronological review of magmatism along the external margin of Columbia and in the Grenville-age orogens forming the core of Rodinia. *Precambrian Res.* **2022**, *371*, 106463. [CrossRef]
14. Wang, W.; Cawood, P.A.; Pandit, M.K.; Xia, X.P.; Raveggi, M.; Zhao, J.H.; Zheng, J.P.; Qi, L. Fragmentation of South China from greater India during the Rodinia-Gondwana transition. *Geology* **2021**, *49*, 228–232. [CrossRef]
15. Wu, P.; Zhang, S.B.; Zheng, Y.F.; Fu, B.; Liang, T. Amalgamation of South China into Rodinia during the Grenvillian accretionary orogeny: Geochemical evidence from Early Neoproterozoic igneous rocks in the northern margin of the South China Block. *Precambrian Res.* **2019**, *321*, 221–243. [CrossRef]
16. Zhou, Z.Y.; Yang, J.X.; Zhou, H.W.; Jiang, L.S. Significance on Hubei Huangling complex in the Rodinia super continent of evolution. *Resour. Environ. Eng.* **2007**, *21*, 380–384.

17. Zhao, J.H.; Li, Q.W.; Liu, H.; Wang, W. Neoproterozoic magmatism in the western and northern margins of the Yangtze Block (South China) controlled by slab subduction and subduction-transform-edge-propagator. *Earth Sci. Rev.* **2018**, *187*, 1–18. [CrossRef]

18. Deng, H.; Kusky, T.M.; Wang, L.; Peng, S.B.; Jiang, X.F.; Wang, J.P.; Wang, S.J. Discovery of a sheeted dike complex in the northern Yangtze craton and its implications for craton evolution. *J. Earth Sci.* **2012**, *23*, 676–695. [CrossRef]

19. Deng, H.; Peng, S.B.; Polat, A.; Timothy, M.K.; Jiang, X.F.; Han, Q.S.; Wang, L.; Huang, Y.; Wang, J.P.; Zeng, W.; et al. Neoproterozoic IAT intrusion into Mesoproterozoic MOR Miaowan Ophiolite, Yangtze Craton: Evidence for evolving tectonic settings. *Precambrian Res.* **2017**, *289*, 75–94. [CrossRef]

20. Jiang, X.F.; Peng, S.B.; Han, Q.S. Petrogenesis and Geological Significance of ca. 860 Ma Dikes in Southern Huangling Anticline, Yangtze Craton. *Earth Sci.* **2021**, *46*, 2117–2132.

21. Jiang, X.f.; Peng, S.B.; Kusky, T.M.; Wang, L.; Deng, H. Petrogenesis and Geotectonic Significance of Early-Neoproterzoic Olivine-Gabbro within the Yangtze Craton: Constrains from the Mineral Composition, U-Pb Age and Hf Isotopes of Zircons. *J. Earth Sci.* **2018**, *29*, 93–102. [CrossRef]

22. Peng, M.; Wu, Y.B.; Gao, S.; Zhang, H.f.; Wang, J.; Liu, X.C.; Gong, H.J.; Zhou, L.; Hu, Z.C.; Liu, Y.S.; et al. Geochemistry, zircon U–Pb age and Hf isotope compositions of Paleoproterozoic aluminous A-type granites from the Kongling terrain, Yangtze Block: Constraints on petrogenesis and geologic implications. *Gondwana Res.* **2012**, *22*, 140–151. [CrossRef]

23. Peng, S.B.; Kusky, T.M.; Jiang, X.F.; Wang, L.; Wang, J.P.; Deng, H. Geology, geochemistry, and geochronology of the Miaowan ophiolite, Yangtze craton: Implications for South China's amalgamation history with the Rodinian supercontinent. *Gondwana Res.* **2012**, *21*, 577–594. [CrossRef]

24. Cui, X.; Zhu, W.B.; Wang, X. Neoproterozoic modification of heterogeneous continental lithosphere beneath the Yangtze interior: Revealed from mafic dykes from the Huangling area, South China. *Int. J. Earth Sci. (Geol. Rundsch.)* **2021**, *111*, 27–51. [CrossRef]

25. Wei, Y.X.; Peng, S.B.; Jiang, X.F.; Peng, Z.Q.; Peng, L.H.; Li, Z.H.; Zhou, P.; Zeng, X.W. SHRIMP zircon U-Pb ages and geochemical characteristics of the neoproterozoic granitoids in the Huangling anticline and its tectonic setting. *J. Earth Sci.* **2012**, *23*, 659–676. [CrossRef]

26. Zhao, J.H.; Zhou, M.F.; Zheng, J.P. Neoproterozoic high-K granites produced by melting of newly formed mafic crust in the Huangling region, South China. *Precambrian Res.* **2013**, *233*, 93–107. [CrossRef]

27. Zhao, J.H.; Zhou, M.F.; Zheng, J.P.; Griffin, W.L. Neoproterozoic tonalite and trondhjemite in the Huangling complex, South China: Crustal growth and reworking in a continental arc environment. *Am. J. Sci.* **2013**, *313*, 540–583. [CrossRef]

28. Zhang, Q.; Wang, Y.L.; Jin, W.J.; Jia, X.Q.; Li, C.D. Criteria for the recognition of pre-, syn-and post-orogenic granitic rocks. *Geolocial Bull. China* **2008**, *27*, 1–18.

29. Pearce, J.A.; Peate, D.W. Tectonic implications of the composition of volcanic arc magmas. *Annu. Rev. Earth Planet. Sci.* **1995**, *23*, 251–285. [CrossRef]

30. Chappell, B.W.; White, A.J.R. I-Type and S-Type Granites in the Lachlan Fold Belt. *Trans. R. Soc. Edinb.-Earth Sci.* **1992**, *83*, 1–26.

31. Whalen, J.B.; Currie, K.L.; Chappell, B.W. A-type granites: Geochemical characteristics, discrimination and petrogenesis. *Contrib. Mineral. Petrol.* **1987**, *95*, 407–419. [CrossRef]

32. Pearce, J.A. Sources and settings of granitic rocks. *Int. Union Geol. Sci.* **1996**, *19*, 120–125. [CrossRef]

33. Sylvester, P.J. Post-Collisional Alkaline Granites. *J. Geol.* **1989**, *97*, 261–280. [CrossRef]

34. Carvalho, P.C.S.; Neiva, A.M.R.; Silva, M.M.V.G.; Corfu, F. A unique sequential melting mechanism for the generation of anatectic granitic rocks from the Penafiel area, northern Portugal. *Lithos* **2012**, *155*, 110–124. [CrossRef]

35. Gao, S.; Ling, W.L.; Qiu, Y.M.; Lian, Z.; Gerald, H.; Klaus, S. Contrasting geochemical and Sm-Nd isotopic compositions of Archean metasediments from the Kongling high-grade terrain of the Yangtze craton evidence for cratonic evolution and redistribution of REE during crustal anatexis. *Geochim. Cosmochim. Acta* **1999**, *63*, 2071–2088. [CrossRef]

36. Gao, S.; Yang, J.; Zhou, L.; Li, M.; Hu, Z.C.; Guo, J.L.; Yuan, H.L.; Gong, H.J.; Xiao, G.Q.; Wei, J.Q. Age and growth of the Archean Kongling terrain, South China, with emphasis on 3.3 ga granitoid gneisses. *Am. J. Sci.* **2011**, *311*, 153–182. [CrossRef]

37. Guo, J.L.; Gao, S.; Wu, Y.B.; Li, M.; Chen, K.; Hu, Z.C.; Liang, Z.W.; Liu, Y.S.; Zhou, L.; Zong, K.Q.; et al. 3.45Ga granitic gneisses from the Yangtze Craton, South China: Implications for Early Archean crustal growth. *Precambrian Res.* **2014**, *242*, 82–95. [CrossRef]

38. Ling, W.; Gao, S.; Cheng, J.; Jiang, L.; Yuan, H.; Hu, Z. Neoproterozoic magmatic events within the Yangtze continental interior and along its northern margin and their tectonic implication: Constraint from the ELA-ICPMS U-Pb geochronogy of zicrons from the Huangling and Hannan complexes. *Acta Petrol. Sin.* **2006**, *22*, 387–396.

39. Li, H.Q.; Zhou, W.X.; Wei, Y.X.; Chang, F.; Wang, B.; Tan, M.T.; Hu, Z.X.; Xu, D.L.; Liu, H. Two extensional events in the early evolution of the Yangtze Block, South China: Geochemical and isotopic evidence from two sets of Paleoproterozoic alkali porphyry in the Northern Kongling terrane. *Geol. J.* **2020**, *55*, 6296–6324. [CrossRef]

40. Zhou, H.; Zhou, W.X.; Wei, Y.X.; Fru, E.C.; Huang, B.; Fu, D.; Li, H.Q.; Tan, M.T. Mesoarchean banded iron-formation from the northern Yangtze Craton, South China and its geological and paleoenvironmental implications. *Precambrian Res.* **2022**, *383*, 106905. [CrossRef]

41. Zhou, W.X.; Huang, B.; Wei, Y.X.; Li, H.Q.; Tan, M.T.; Fu, D. Paleoproterozoic ophiolitic melanges and orogenesis in the northern Yangtze Craton: Evidence for the operation of modern-style plate tectonics. *Precambrian Res.* **2021**, *364*, 106385. [CrossRef]

42. Han, Q.S.; Peng, S.B. Paleoproterozoic subduction within the Yangtze Craton: Constraints from Nb-enriched mafic dikes in the Kongling complex. *Precambrian Res.* **2020**, *340*, 105634. [CrossRef]
43. Han, Q.S.; Peng, S.B.; Kusky, T.; Polat, A.; Jiang, X.F.; Cen, Y.; Liu, S.F.; Deng, H. A Paleoproterozoic ophiolitic melange, Yangtze craton, South China: Evidence for Paleoproterozoic suturing and microcontinent amalgamation. *Precambrian Res.* **2017**, *293*, 13–38. [CrossRef]
44. Han, Q.S.; Peng, S.B.; Polat, A.; Kusky, T. Petrogenesis and geochronology of Paleoproterozoic magmatic rocks in the Kongling complex: Evidence for a collisional orogenic event in the Yangtze craton. *Lithos* **2019**, *342*, 513–529. [CrossRef]
45. Wei, J.Q. Petrology and geochemistry of the Archean Huangling greenstone belt in the Yangtze Craton, South China. *Precambrian Res.* **2021**, *364*, 106340. [CrossRef]
46. Wei, J.Q.; Wei, Y.X.; Wang, J.X.; Wang, X.D. Geochronological constraints on the formation and evolution of the Huangling basement in the Yangtze craton, South China. *Precambrian Res.* **2020**, *342*, 105707. [CrossRef]
47. Li, H.; Wei, Y.; Zhou, W.; Chi Fru, E.; Drüppel, K.; Xu, D.; Deng, X.; Liu, H.; Tan, M. A Neoproterozoic appinite rock suite records the early tectonic evolution of the northern margin of the Yangtze Block during convergence with Rodinia. *Precambrian Res.* **2024**, *409*, 107448. [CrossRef]
48. Ma, D.Q.; Du, S.H.; Xiao, Z.F. The origin of Huangling granite batholith. *Acta Petrol. Mineral.* **2002**, *21*, 151–161.
49. Feng, D.y.; Lin, Z.c.; Zhang, Z.c. Intrusive ages and isotopic characteristics of massives in the south of Huangling granitoids. *Resour. Environ. Eng.* **1991**, *5*, 1–12.
50. Li, X.H.; Li, Z.X.; Ge, W.H.; Zhou, H.W.; Li, W.X.; Liu, Y. U-Pb zircon ages of the Neoproterozoic granitoids in south China and their tectonic implications. *Bull. Mineral. Petrol. Geochem.* **2001**, *4*, 271–273.
51. Li, Y.L.; Zhou, H.W.; Li, X.H.; Luo, Q.H. 40Ar-39Ar plateau ages of biotite and amphibole from tonalite of Huangling granitoids and their cooling curve. *Acta Petrol. Sin.* **2007**, *23*, 1067–1074.
52. Zhang, S.B.; Zheng, Y.F.; Zhao, Z.F.; Wu, Y.B.; Yuan, H.L.; Wu, F.Y. Origin of TTG-like rocks from anatexis of ancient lower crust: Geochemical evidence from Neoproterozoic granitoids in South China. *Lithos* **2009**, *113*, 347–368. [CrossRef]
53. Ma, G.G.; Li, H.Q.; Zhang, Z.C. Study on the Limits of Sinian Time in South China. *J. Yichang Inst. Geol. Miner. Resour.* **1984**, *8*.
54. Gao, S.; Zhang, B.R.; Li, Z.J. Geochemical evidence for Proterozoic continental arc and continental-margin rift magmatism along the northern margin of the Yangtze Craton, South China. *Precambrian Res.* **1990**, *47*, 205–221.
55. Li, X.H.; Li, Z.X.; Ge, W.C.; Zhou, H.W.; Li, W.X.; Liu, Y.; Wingate, M.T.D. Neoproterozoic granitoids in South China: Crustal melting above a mantle plume at ca. 825 Ma? *Precambrian Res.* **2003**, *122*, 45–83. [CrossRef]
56. Li, Z.X.; Li, X.H.; Kinny, P.D.; Wang, J. The breakup of Rodinia: Did it start with a mantle plume beneath South China? *Earth Planet. Sci. Lett.* **1999**, *173*, 171–181. [CrossRef]
57. Han, Q.S.; Peng, S.B.; Polat, A.; Kusky, T.; Deng, H.; Wu, T.Y. A ca.2.1 Ga Andean-type margin built on metasomatized lithosphere in the northern Yangtze craton, China: Evidence from high-Mg basalts and andesites. *Precambrian Res.* **2018**, *309*, 309–324. [CrossRef]
58. Qiu, X.F.; Ling, W.L.; Liu, X.M.; Lu, S.S.; Jiang, T.; Wei, Y.X.; Peng, L.H.; Tan, J.J. Evolution of the Archean continental crust in the nucleus of the Yangtze block: Evidence from geochemistry of 3.0 Ga TTG gneisses in the Kongling high-grade metamorphic terrane, South China. *J. Asian Earth Sci.* **2018**, *154*, 149–161. [CrossRef]
59. Jiang, X.F.; Peng, S.B.; Polat, A.; Kusky, T.; Wang, L.; Wu, T.Y.; Lin, M.S.; Han, Q.S. Geochemistry and geochronology of mylonitic metasedimentary rocks associated with the Proterozoic Miaowan Ophiolite Complex, Yangtze craton, China: Implications for geodynamic events. *Precambrian Res.* **2016**, *279*, 37–56. [CrossRef]
60. Ludwig, K.R. User's Manual for Isoplot/Ex, Version 3.00, a Geochronological Toolkit for Microsoft Excel. Berkeley Geochronology Center Special Publications: Berkeley, CA, USA, 2003.
61. Williams, I.S. U-Th-Pb Geochronology by Ion Microprobe. *Rev. Econ. Geol.* **1998**, *7*, 1–35.
62. Wan, Y.s.; Li, R.W.; Wilde, S.A.; Liu, D.Y.; Chen, Z.Y.; Yan, L.; Song, T.R.; Yin, X.Y. UHP metamorphism and exhumation of the Dabie Orogen, China: Evidence from SHRIMP dating of zircon and monazite from a UHP granitic gneiss cobble from the Hefei Basin. *Geochim. Cosmochim. Acta* **2005**, *69*, 4333–4348. [CrossRef]
63. Claoué-Long, J.C.; Zhang, Z.C.; Ma, G.G.; Du, S.H. The age of the Permian-Triassic boundary. *Earth Planet. Sci. Lett.* **1991**, *105*, 182–190. [CrossRef]
64. Wu, F.Y.; Yang, Y.H.; Xie, L.W.; Yang, J.H.; Xu, P. Hf isotopic compositions of the standard zircons and baddeleyites used in U–Pb geochronology. *Chem. Geol.* **2006**, *234*, 105–126. [CrossRef]
65. Black, L.P.; Kamo, S.L.; Williams, I.S.; Mundil, R.; Davis, D.W.; Korsch, R.J.; Foudoulis, C. The application of SHRIMP to Phanerozoic geochronology; a critical appraisal of four zircon standards. *Chem. Geol.* **2003**, *200*, 171–188. [CrossRef]
66. Hou, K.J.; Li, Y.H.; Zou, T.R.; Qu, X.M.; Shi, Y.R.; Xie, G.Q. Laser ablation-MC-ICP-MS technique for Hf isotope microanalysis of zircon and its geological applications. *Acta Petrol. Sin.* **2007**, *23*, 2595–2604.
67. Chu, N.C.; Taylor, R.N.; Chavagnac, V.; Nesbitt, R.W.; Boella, R.M.; Milton, J.A.; German, C.R.; Bayon, G.; Burton, K. Hf isotope ratio analysis using multi-collector inductively coupled plasma mass spectrometry: An evaluation of isobaric interference corrections. *J. Anal. At. Spectrom.* **2002**, *17*, 1567–1574. [CrossRef]
68. Elhlou, S.; Belousova, E.; Griffin, W.L.; Pearson, N.J.; O'Reilly, S.Y. Trace element and isotopic composition of GJ-red zircon standard by laser ablation. *Geochim. Cosmochim. Acta* **2006**, *70*, A158. [CrossRef]
69. Li, H.Q. Study on Rb-Sr isotopic ages of gold deposits in West Junggar area, Xinjiang. *Acta Geol. Sin.* **2000**, *74*, 181–192.

70. Ma, D.Q.; Li, Z.C.; Xiao, Z.F. The constitute, geochronology and geologic evolution of the Kongling complex, western Hubei. *Acta Geosci. Sin.* **1997**, *18*, 233–241.

71. Cherniak, D.J.; Watson, E.B. Pb diffusion in zircon. *Chem. Geol.* **2001**, *172*, 5–24. [CrossRef]

72. Le Maitre, R.W.B.; Dudek, P.; Keller, A.; Lameyre, J.; Le Bas, J.; Sabine, M.J.; Schmid, P.A.; Sorensen, R.; Streckeisen, H.; Woolley, A. A Classification of Igneous Rocks and Glossary of Terms: Recommendations of the International Union of Geological Sciences, Subcommission on the Systematics of Igneous Rocks. International Union of Geological Sciences: Paris, France, 1989.

73. Le Maitre, R.W.; Streckeisen, A.; Zanettin, B.; Le Bas, M.; Bonin, B.; Bateman, P. *Igneous Rocks: A Classification and Glossary of Terms*; Cambridge University Press: Cambridge, UK, 2005.

74. Peccerillo, A.; Taylor, S. Geochemistry of Eocene calc-alkaline volcanic rocks from the Kastamonu area, northern Turkey. *Contrib. Mineral. Petrol.* **1976**, *58*, 63–81. [CrossRef]

75. Maniar, P.D.; Piccoli, P.M. Tectonic discrimination of granitoids. *Geol. Soc. Am. Bull.* **1989**, *101*, 635–643. [CrossRef]

76. Frost, B.R.; Barnes, C.G.; Collins, W.J.; Arculus, R.J.; Ellis, D.J.; Frost, C.D. A geochemical classification for granitic rocks. *J. Petrol.* **2001**, *42*, 2033–2048. [CrossRef]

77. Sun, S.S.; McDonough, W.F. Chemical and isotopic systematics of oceanic basalts: Implications for mantle composition and processes. *Geol. Soc. Lond. Spec. Publ.* **1989**, *42*, 313–345. [CrossRef]

78. Vervoort, J.D.; Patchett, P.J. Behaviour of hafnium and neodymium isotopes in the crust: Constraints from Precambrian crustally derived granites. *Geochim. Cosmochim. Acta* **1996**, *60*, 3717–3733. [CrossRef]

79. Gao, S.; Rudnick, R.L.; Yuan, H.L.; Liu, X.M.; Liu, Y.S.; Xu, W.L.; Ling, W.L.; Ayers, J.; Wang, X.C.; Wang, Q.H. Recycling lower continental crust in the North China craton. *Nature* **2004**, *432*, 892–897. [CrossRef] [PubMed]

80. Streckeisen, A.L. Classification and nomenclature of igneous rocks. Recommendation of the IUGS subcomision on the systematic of igneous rocks. *Geol. Rundsch* **1974**, *6*, 773–786. [CrossRef]

81. Skjerlie, K.P.; Johnston, A.D. Fluid-absent melting behavior of an F-rich tonalitic gneiss at mid-crustal pressures: Implications for the generation of anorogenic granites. *J. Petrol.* **1993**, *34*, 785–815. [CrossRef]

82. Douce, A.E.P. Generation of metaluminous A-type granites by low-pressure melting of calc-alkaline granitoids. *Geology* **1997**, *25*, 743–746. [CrossRef]

83. Castro, A.; Morenoventas, I.; Delarosa, J.D. H-type (hybrid) granitoids: A proposed revision of the granite-type classification and nomenclature. *Earth Sci. Rev.* **1991**, *31*, 237–253. [CrossRef]

84. Sisson, T.W.; Ratajeski, K.; Hankins, W.B.; Glazner, A.F. Voluminous granitic magmas from common basaltic sources. *Contrib. Mineral. Petrol.* **2005**, *148*, 635–661. [CrossRef]

85. Clemens, J.D. Granitic magmas with I-type affinities, from mainly metasedimentary sources: The Harcourt batholith of southeastern Australia. *Contrib. Mineral. Petrol.* **2018**, *173*, 93. [CrossRef]

86. Clemens, J.D.; Stevens, G.; Farina, F. The enigmatic sources of I-type granites: The peritectic connexion. *Lithos* **2011**, *126*, 174–181. [CrossRef]

87. Cawthorn, R.G.; Strong, D.; Brown, P. Origin of corundum-normative intrusive and extrusive magmas. *Nature* **1976**, *259*, 102–104. [CrossRef]

88. Defant, M.J.; Drummond, M.S. Derivation of some modern arc magmas by melting of young subducted lithosphere. *Nature* **1990**, *347*, 662. [CrossRef]

89. Chappell, B.W. Compositional variation within granite suites of the Lachlan fold belt: Its causes and implications for the physical state of granite magma. *Trans. R. Soc. Edinb. Earth Sci.* **1996**, *87*, 159–170.

90. Bonin, B. Do coeval mafic and felsic magmas in post-collisional to within-plate regimes necessarily imply two contrasting, mantle and crustal, sources? A review. *Lithos* **2004**, *78*, 1–24. [CrossRef]

91. Kocak, K.; Zedef, V.; Kansun, G. Magma mixing/mingling in the Eocene Horoz (Nigde) granitoids, Central southern Turkey: Evidence from mafic microgranular enclaves. *Mineral. Petrol.* **2011**, *103*, 149–167. [CrossRef]

92. Lameyre, J.; Bowden, P. Plutonic rock types series: Discrimination of various granitoid series and related rocks. *J. Volcanol. Geotherm. Res.* **1982**, *14*, 169–186. [CrossRef]

93. Collins, W.J.; Beams, S.D.; White, A.J.R.; Chappell, B.W. Nature and origin of A-type granites with particular reference to southeastern Australia. *Contrib. Mineral. Petrol.* **1982**, *80*, 189–200. [CrossRef]

94. Rudnick, R.L.; Barth, M.; Horn, I.; McDonough, W.F. Rutile-bearing refractory eclogites: Missing link between continents and depleted mantle. *Science* **2000**, *287*, 278–281. [CrossRef] [PubMed]

95. Rudnick, R.L.; McLennan, S.M.; Taylor, S.R. Large ion lithophile elements in rocks from high-pressure granulite facies terrains. *Geochim. Cosmochim. Acta* **1985**, *49*, 1645–1655. [CrossRef]

96. Xiong, Q.; Zheng, J.P.; Yu, C.M.; Su, Y.P.; Tang, H.Y.; Zhang, Z.H. Zircon U-Pb age and Hf isotope of Quanyishang A-type granite in Yichang: Signification for the Yangtze continental cratonization in Paleoproterozoic. *Chin. Sci. Bull.* **2009**, *54*, 436–446. [CrossRef]

97. Chen, K.; Gao, S.; Wu, Y.B.; Guo, J.L.; Hu, Z.C.; Liu, Y.S.; Zong, K.Q.; Liang, Z.W.; Geng, X.L. 2.6–2.7Ga crustal growth in Yangtze craton, South China. *Precambrian Res.* **2013**, *224*, 472–490. [CrossRef]

98. Guo, J.W.; Zheng, J.P.; Cawood, P.A.; Weinberg, R.F.; Ping, X.Q.; Li, Y.H. Archean trondhjemitic crust at depth in Yangtze Craton: Evidence from TTG xenolith in mafic dyke and apatite inclusion pressure in zircon. *Precambrian Res.* **2021**, *354*, 106055. [CrossRef]

99. Guo, J.W.; Zheng, J.Q.; Ping, X.Q.; Wan, Y.S.; Li, Y.H.; Wu, Y.B.; Zhao, J.H.; Wang, W. Paleoproterozoic porphyries and coarse-grained granites manifesting a vertical hierarchical structure of Archean continental crust beneath the Yangtze Craton. *Precambrian Res.* **2018**, *314*, 288–305. [CrossRef]

100. Wei, Y.X.; Zhou, W.X.; Hu, Z.X.; Li, H.Q.; Huang, X.X.; Zhao, X.M.; Xu, D.L. Geochronology and Geochemistry of Archean TTG and Tremolite Schist Xenoliths in Yemadong Complex: Evidence for >= 3.0 Ga Archean Continental Crust in Kongling High-Grade Metamorphic Terrane, Yangtze Craton, China. *Minerals* **2019**, *9*, 689. [CrossRef]

101. Zhang, S.B.; Zheng, Y.F.; Zhao, Z.F.; Wu, Y.B.; Yuan, H.L.; Wu, F.Y. Neoproterozoic anatexis of Archean lithosphere: Geochemical evidence from felsic to mafic intrusions at Xiaofeng in the Yangtze Gorge, South China. *Precambrian Res.* **2008**, *163*, 210–238. [CrossRef]

102. Green, T.H. Significance of Nb/Ta as an indicator of geochemical processes in the crust-mantle system. *Chem. Geol.* **1995**, *120*, 347–359. [CrossRef]

103. Tang, M.; Lee, C.-T.A.; Chen, K.; Erdman, M.; Costin, G.; Jiang, H. Nb/Ta systematics in arc magma differentiation and the role of arclogites in continent formation. *Nat. Commun.* **2019**, *10*, 235. [CrossRef] [PubMed]

104. Gibson, S.A.; Thompson, R.N.; Dickin, A.P.; Leonardos, O.H. High-Ti and low-Ti mafic potassic magmas: Key to plume-lithosphere interactions and continental flood-basalt genesis. *Earth Planet. Sci. Lett.* **1995**, *136*, 149–165. [CrossRef]

105. Frey, F.A.; Green, D.H.; Roy, S.D. Integrated Models of Basalt Petrogenesis: A Study of Quartz Tholeiites to Olivine Melilitites from South Eastern Australia Utilizing Geochemical and Experimental Petrological Data. *J. Petrol.* **1978**, *19*, 463–513. [CrossRef]

106. Wu, F.y.; Li, X.h.; Zheng, Y.f.; Gao, S. Lu-Hf isotopic systematics and their applications in petrology. *Acta Petrol. Sin.* **2007**, *23*, 185–220.

107. Du, L.; Long, X.P.; Yuan, C.; Zhang, Y.Y.; Huang, Z.Y.; Wang, X.Y.; Yang, Y.H. Mantle contribution and tectonic transition in the Aqishan-Yamansu Belt, Eastern Tianshan, NW China: Insights from geochronology and geochemistry of Early Carboniferous to Early Permian felsic intrusions. *Lithos* **2018**, *304*, 230–244. [CrossRef]

108. Wang, Y.H.; Xue, C.J.; Liu, J.J.; Zhang, F.F. Geological, geochronological, geochemical, and Sr-Nd-O-Hf isotopic constraints on origins of intrusions associated with the Baishan porphyry Mo deposit in eastern Tianshan, NW China. *Miner. Depos.* **2016**, *51*, 953–969. [CrossRef]

109. Griffin, W.L.; Wang, X.; Jackson, S.E.; Pearson, N.J.; O'Reilly, S.Y.; Xu, X.s.; Zhou, X.m. Zircon chemistry and magma mixing, SE China: In-situ analysis of Hf isotopes, Tonglu and Pingtan igneous complexes. *Lithos* **2002**, *61*, 237–269. [CrossRef]

110. Qiu, J.S.; Liu, L.; LI, Z. Zircon U-Pb geochronology and Sr-Nd-Hf isotopic geochemistry of quartz syenite from Wanghaigang pluton in Huangyan County, Zhejiang Province and their implications for petrogenesis. *Acta Petrol. Sin.* **2011**, *27*, 1557–1572.

111. Pitcher, W.S. Granites and yet more granites forty years on. *Geol. Rundsch.* **1987**, *76*, 51–79. [CrossRef]

112. Roberts, M.P.; Clemens, J.D. Origin of high-potassium, calc-alkaline, I-type granitoids. *Geology* **1993**, *21*, 825–828. [CrossRef]

113. Wu, F.Y.; Li, X.H.; Yang, J.H.; Zheng, Y.F. Discussions on the petrogenesis of granites. *Acta Petrol. Sin.* **2007**, *23*, 1217–1238.

114. Wu, H.; Zhang, Y.H.; Ling, W.L.; Bai, X.; Ma, Q.; Berkana, W.F.; Cheng, J.P.; Peng, L.H. Recognition of mantle input and its tectonic implication for the nature of ~815 Ma magmatism in the Yangtze continental interior, South China. *Precambrian Res.* **2016**, *279*, 17–36. [CrossRef]

115. Jakeš, P.; White, A.R. Major and trace element abundances in volcanic rocks of orogenic areas. *Geol. Soc. Am. Bull.* **1972**, *83*, 29–40. [CrossRef]

116. Arculus, R.J.; Powell, R. Source component mixing in the regions of arc magma generation. *J. Geophys. Res. Solid Earth* **1986**, *91*, 5913–5926. [CrossRef]

117. Rino, S.; Kon, Y.; Sato, W.; Maruyama, S.; Santosh, M.; Zhao, D. The Grenvillian and Pan-African orogens: World's largest orogenies through geologic time, and their implications on the origin of superplume. *Gondwana Res.* **2008**, *14*, 51–72. [CrossRef]

118. Gregory, L.C.; Meert, J.G.; Bingen, B.; Pandit, M.K.; Torsvik, T.H. Paleomagnetism and geochronology of the Malani Igneous Suite, Northwest India: Implications for the configuration of Rodinia and the assembly of Gondwana. *Precambrian Res.* **2009**, *170*, 13–26. [CrossRef]

119. Bybee, G.M.; Ashwal, L.D.; Wilson, A.H. New evidence for a volcanic arc on the western margin of a rifting Rodinia from ultramafic intrusions in the Andriamena region, north-central Madagascar. *Earth Planet. Sci. Lett.* **2010**, *293*, 42–53. [CrossRef]

120. Hui, B.; Dong, Y.P.; Zhang, F.F.; Sun, S.S.; He, S. Petrogenesis and tectonic implications of the Neoproterozoic mafic intrusions in the Bikou Terrane along the northwestern margin of the Yangtze Block, South China. *Ore Geol. Rev.* **2021**, *131*, 104014. [CrossRef]

121. Zhang, X.q.; Zhang, H.f.; Zou, H.b. Rift-related Neoproterozoic tholeiitic layered mafic intrusions at northern Yangtze Block, South China: Mineral chemistry evidence. *Lithos* **2020**, *356*, 105376. [CrossRef]

122. Zou, H.; Li, Y.; Huang, C.C.; Said, N.; Jiang, X.W.; Liu, H.; Li, M.; Chen, H.F.; Liu, C.M.; Lan, Z.W. Ca. 815 Ma intra-plate granitoids and mafic dykes from Emeishan pluton in the western Yangtze Block, SW China: A record of rifting during the breakup of Rodinia. *Precambrian Res.* **2022**, *371*, 106569. [CrossRef]

123. Zhu, Y.; Lai, S.C.; Qin, J.F.; Zhu, R.Z.; Liu, M.; Zhang, F.Y.; Zhang, Z.Z.; Yang, H. Neoproterozoic metasomatized mantle beneath the western Yangtze Block, South China: Evidence from whole-rock geochemistry and zircon U-Pb-Hf isotopes of mafic rocks. *J. Asian Earth Sci.* **2021**, *206*, 104616. [CrossRef]

124. Gao, L.E.; Zeng, L.S.; Zhao, L.H.; Yan, L.L. Sequential melting of deep crustal source rocks in a rift system: An example from southern Tibet. *Chem. Geol.* **2023**, *618*, 121295. [CrossRef]

125. McLelland, J.; Daly, J.S.; McLelland, J.M. The Grenville orogenic cycle (ca. 1350-1000 Ma): An Adirondack perspective. *Tectonophysics* **1996**, *265*, 1–28. [CrossRef]

126. Moore, J.M., Jr.; Thompson, P.H. The Flinton Group: A late Precambrian metasedimentary succession in the Grenville Province of eastern Ontario. *Can. J. Earth Sci.* **1980**, *17*, 1685–1707. [CrossRef]

127. Chiarenzelli, J.R.; McLelland, J.M. Age and regional relationships of granitoid rocks of the Adirondack Highlands. *J. Geol.* **1991**, *99*, 571–590. [CrossRef]

128. Zhou, G.Y.; Wu, Y.B.; Zhang, W.X.; He, Y. Circa 900 Ma low δ18O A-type rhyolite in the northern Yangtze Block: Genesis and geological significance. *Precambrian Res.* **2019**, *324*, 155–169. [CrossRef]

129. Wang, R.R.; Xu, Z.Q.; Santosh, M.; Zeng, B. Mid-Neoproterozoic magmatism in the northern margin of the Yangtze Block, South China: Implications for transition from subduction to post-collision. *Precambrian Res.* **2021**, *354*, 106073. [CrossRef]

130. Huang, C.C.; Zou, H.; Bagas, L.; Chen, H.F.; Xiao, B.; Jiang, X.W.; Li, M.; Hu, C.H.; Yu, L.M. Mid-Neoproterozoic tectonic evolution of the northern margin of the Yangtze Block, South China: New insights from high-temperature magma events. *Lithos* **2022**, *420–421*, 106711. [CrossRef]

131. Hu, J.; Liu, X.C.; Qu, W.; Chen, L.Y. Mid-Neoproterozoic amphibolite facies metamorphism at the northern margin of the Yangtze craton. *Precambrian Res.* **2019**, *326*, 333–343. [CrossRef]

132. Zhang, R.Y.; Sun, Y.; Zhang, X.; Ao, W.H.; Santosh, M. Neoproterozoic magmatic events in the South Qinling Belt, China: Implications for amalgamation and breakup of the Rodinia supercontinent. *Gondwana Res.* **2016**, *30*, 6–23. [CrossRef]